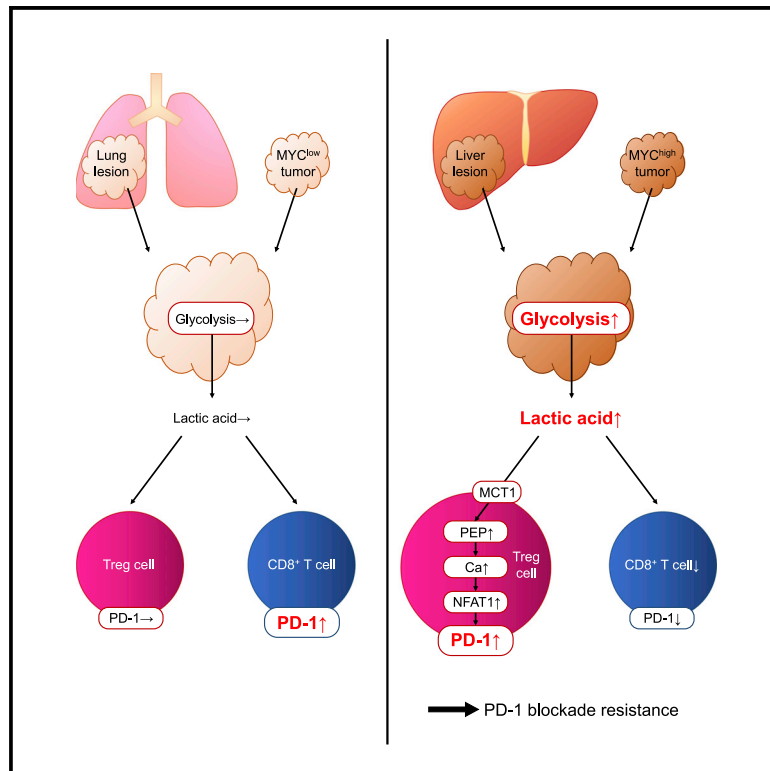# Lactic acid promotes PD-1 expression in regulatory T cells in highly glycolytic tumor microenvironments

Graphical abstract

Highlights

- LA induces PD-1 expression by Treg cells in highly glycolytic tumors

- LA absorbed through MCT1 is a metabolic checkpoint of immune responses

- *MYC*-amplified or liver metastatic tumors augment PD-1^{+} Treg cells with abundant LA

- MCT1 highly expressed by Treg cells provides therapeutic target for immunotherapy

Authors

Shogo Kumagai, Shohei Koyama, Kota Itahashi, ..., Kohei Shitara, Hiroyuki Mano, Hiroyoshi Nishikawa

Correspondence

skoyama@east.ncc.go.jp (S.K.), hnishika@ncc.go.jp (H.N.)

In brief

Kumagai et al. show that Treg cells uptake lactic acid in the highly glycolytic tumor microenvironment via MCT1 and robustly express PD-1, resulting in the impairment of PD-1 blockade therapy.

CellPress

Article

Lactic acid promotes PD-1 expression in regulatory T cells in highly glycolytic tumor microenvironments

Shogo Kumagai,[1,2,3] Shohei Koyama,[2,4,*] Kota Itahashi,[2] Tokiyoshi Tanegashima,[2] Yi-tzu Lin,[2,3] Yosuke Togashi,[2] Takahiro Kamada,[2] Takuma Irie,[2] Genki Okumura,[2] Hidetoshi Kono,[2] Daisuke Ito,[2] Rika Fujii,[2] Sho Watanabe,[2] Atsuo Sai,[2,3] Shota Fukuoka,[2] Eri Sugiyama,[2] Go Watanabe,[2] Takuya Owari,[2] Hitomi Nishinakamura,[2] Daisuke Sugiyama,[3] Yuka Maeda,[2] Akihito Kawazoe,[5] Hiroki Yukami,[5] Keigo Chida,[5] Yuuki Ohara,[6] Tatsuya Yoshida,[7] Yuki Shinno,[7] Yuki Takeyasu,[7] Masayuki Shirasawa,[7] Kenta Nakama,[8] Keiju Aokage,[9] Jun Suzuki,[9] Genichiro Ishii,[6] Takeshi Kuwata,[6] Naoya Sakamoto,[6] Masahito Kawazu,[1] Toshihide Ueno,[1] Taisuke Mori,[10] Naoya Yamazaki,[8] Masahiro Tsuboi,[9] Yasushi Yatabe,[10] Takahiro Kinoshita,[11] Toshihiko Doi,[5] Kohei Shitara,[5] Hiroyuki Mano,[1] and Hiroyoshi Nishikawa[2,3,12,*]

[1]Division of Cellular Signaling, National Cancer Center Research Institute, Tokyo 104-0045, Japan
[2]Division of Cancer Immunology, Research Institute/Exploratory Oncology Research & Clinical Trial Center (EPOC), National Cancer Center, Tokyo 104-0045/Chiba 277-8577, Japan
[3]Department of Immunology, Nagoya University Graduate School of Medicine, Nagoya 466–8550, Japan
[4]Department of Respiratory Medicine and Clinical Immunology, Osaka University Graduate School of Medicine, Osaka 565–0871, Japan
[5]Department of Gastroenterology and Gastrointestinal Oncology, National Cancer Center Hospital East, Chiba 277-8577, Japan
[6]Pathology and Clinical Laboratories, National Cancer Center Hospital East, Chiba 277-8577, Japan
[7]Department of Thoracic Oncology, National Cancer Center Hospital, Tokyo 104-0045, Japan
[8]Department of Dermatologic Oncology, National Cancer Center Hospital, Tokyo 104-0045, Japan
[9]Department of Thoracic Surgery, National Cancer Center Hospital East, Chiba 277-8577, Japan
[10]Department of Pathology, National Cancer Center Hospital, Tokyo 104-0045, Japan
[11]Department of Gastric Surgery, National Cancer Center Hospital East, Chiba 277-8577, Japan
[12]Lead contact
*Correspondence: skoyama@east.ncc.go.jp (S.K.), hnishika@ncc.go.jp (H.N.)
https://doi.org/10.1016/j.ccell.2022.01.001

SUMMARY

The balance of programmed death-1 (PD-1)-expressing CD8^{+} T cells and regulatory T (Treg) cells in the tumor microenvironment (TME) determines the clinical efficacy of PD-1 blockade therapy through the competition of their reactivation. However, factors that determine this balance remain unknown. Here, we show that Treg cells gain higher PD-1 expression than effector T cells in highly glycolytic tumors, including MYC-amplified tumors and liver tumors. Under low-glucose environments via glucose consumption by tumor cells, Treg cells actively absorbed lactic acid (LA) through monocarboxylate transporter 1 (MCT1), promoting NFAT1 translocation into the nucleus, thereby enhancing the expression of PD-1, whereas PD-1 expression by effector T cells was dampened. PD-1 blockade invigorated the PD-1-expressing Treg cells, resulting in treatment failure. We propose that LA in the highly glycolytic TME is an active checkpoint for the function of Treg cells in the TME via upregulation of PD-1 expression.

INTRODUCTION

Regulatory T (Treg) cells are essential for maintaining immune homeostasis via controlling overactivation and aberrant activation of the immune system (Dominguez-Villar and Hafler, 2018; Li and Rudensky, 2016; Sakaguchi et al., 1995). In tumor immunity, Treg cells suppress effector T cells, including CD8^{+} T cells, which play a vital role in killing cancer cells in the host (Wherry and Kurachi, 2015; Williams and Bevan, 2007). Therefore, the balance between CD8^{+} T cells and Treg cells in the TME is important for the prognosis of various types of cancer (Curiel et al., 2004; Fridman et al., 2012; Sato et al., 2005).

Recent progress of cancer immunotherapy represented by immune checkpoint blockade (ICB) has provided a paradigm shift in cancer therapy across multiple cancer types (Dong et al., 2002; Pardoll, 2012; Zou et al., 2016). However, more than half of patients treated with ICB fail to respond; thus, it is necessary to define biomarkers for selecting responders and to develop more effective cancer immunotherapies. We have recently reported that the PD-1 expression balance between effector T cells and effector Treg (eTreg) cells, which are activated Treg cells, in the TME is a promising predictive biomarker for PD-1 blockade therapy (Kumagai et al., 2020a). Moreover, PD-1^{+} eTreg cells could contribute to hyperprogressive disease after PD-1 blockade in certain patients (Kamada et al., 2019), indicating the importance of the balance of effector T cells and Treg cells also in the therapeutic setting. In line with our reports, some studies have demonstrated that the clinical efficacy of ICB
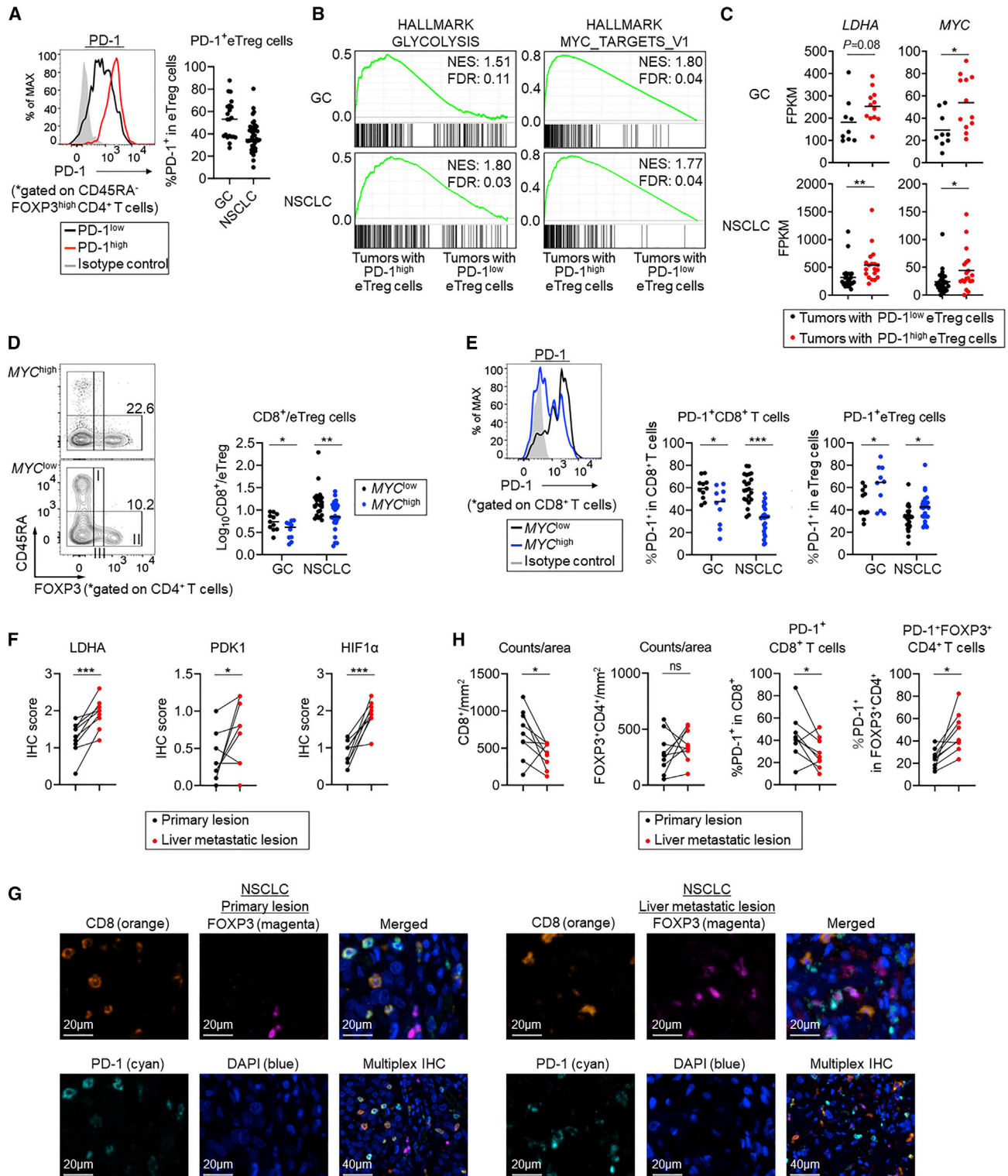
Figure 1. PD-1 expression by eTreg cells is elevated in highly glycolytic tumors

(A–C) Tumor-infiltrating lymphocytes (TILs) from surgically resected GC (cohort 1) and NSCLC (cohort 2) were classified into two subgroups: PD-1^{high} eTreg cells (PD-1 positivity for $\geq$40% of eTreg cells) or PD-1^{low} eTreg cells (PD-1 positivity for <40% of eTreg cells). (A) Representative histogram plots (left) and summary (right) are shown. (B) Glycolysis-related genes and MYC-targeted genes were compared by GSEA between tumors with PD-1^{high} eTreg cells and others. (C) Gene expression of *LDHA* and *MYC* tumors is shown.

(D) Representative contour plots (left) classified according to *MYC* gene expression and summaries (right) are shown.

(legend continued on next page)

varies at different metastatic sites, particularly liver metastatic lesions; this could cause systemic immune tolerance and are lower response to ICB compared with primary lesions (Halabi et al., 2016; Lee et al., 2020; Sasaki et al., 2019a; Topalian et al., 2019; Yu et al., 2021). Moreover, specific gene alterations in *PTEN*, *RHOA*, and *EGFR*, and aberrant oncogenic signaling pathways, such as β-catenin and MYC, in tumor cells contribute to immune escape, leading to resistance to cancer immunotherapy (Koyama et al., 2016; Kumagai et al., 2020b, 2021; Peng et al., 2016; Rooney et al., 2015; Sugiyama et al., 2020).

Tumors mainly utilize glucose to promote aerobic glycolysis for their survival (Warburg effect) (Fantin et al., 2006; Hanahan and Weinberg, 2011). Low-glucose (high-lactic acid [LA]) and hypoxic environments are not suitable for the survival and functions of effector T cells and lead to the decay of antitumor immunity (Gatenby and Gillies, 2004; Ho and Kaech, 2017; Warburg, 1956). Nevertheless, given that Treg cells can abundantly infiltrate and exhibit immunosuppressive functions in the harsh TME, the involvement of distinct metabolic profiles between effector T cells and Treg cells are implicated (Wang et al., 2017). Indeed, Treg cells utilize free fatty acids and LA and keep immunosuppressive function (Angelin et al., 2017; Kumagai et al., 2020b; Watson et al., 2021; Weinberg et al., 2019; Zappasodi et al., 2021).

Here, we address how the balance of PD-1-expressing effector T cells and Treg cells is developed in the TME from the view of metabolic profiles. LA uptake by monocarboxylate transporter 1 (MCT1), which Treg cells predominantly express, promoted NFAT1 translocation into the nucleus and actively induced PD-1 expression. We propose that LA acts as a metabolic checkpoint for Treg cells and controls immune responses in the TME.

RESULTS

Glycolytic activity of tumors is associated with PD-1 expression by eTreg cells in the TME

We investigated factors impacting PD-1 expression by Treg cells in the TME. Treg cells are generally identified with the expression of the master transcription factor FOXP3. In humans, as FOXP3 is also upregulated upon TCR stimulation in naive conventional CD4$^+$ T cells (Tran et al., 2007), activated CD4$^+$ T cells transiently expressing FOXP3 could contaminate *de facto* Treg cells. We, therefore, employed a classification of human Treg cells based on the expression levels of the naive T cell marker CD45RA and FOXP3 (Miyara et al., 2009; Saito et al., 2016; Togashi et al., 2019): naive Treg cells (CD45RA$^+$CD25^{low}FOXP3^{low}CD4$^+$) (I); eTreg cells (CD45RA$^-$CD25^{high}FOXP3^{high}CD4$^+$) (II); and non-Treg cells (CD45RA$^-$CD25^{low}FOXP3^{low}CD4$^+$) (III) (Figure S1A). Gene expression of surgically resected gastric cancer (GC) and non-small cell lung cancer (NSCLC) samples was comprehensively evaluated (Tables S1 and S2) by RNA sequencing (RNA-seq) to clarify the distinctive characteristics of tumors harboring eTreg cells with high PD-1 expression (PD-1^{high} eTreg cells) compared with eTreg cells with low PD-1 expression (PD-1^{low} eTreg cells) (Figure 1A). Gene set enrichment analysis (GSEA) of the RNA-seq data identified significant enrichment of the gene set related to glycolysis and MYC-targeted gene set in tumor tissues from GC and NSCLC harboring PD-1^{high} eTreg cells (Figure 1B). Gene expression of *LDHA* and *MYC* was higher in tumors harboring PD-1^{high} eTreg cells than in tumors with PD-1^{low} eTreg cells (Figure 1C). *MYC* expression significantly associated with a glycolysis signature in our cohort (Figure S1B), consistent with previous reports showing that MYC is a global regulator of glycolysis (Dang et al., 2006; Guo et al., 2000; Kim and Dang, 2006). We closely evaluated the immunological effect of *MYC* expression by tumors. The ratio of tumor-infiltrating CD8$^+$ T cells to eTreg cells and PD-1 expression by tumor-infiltrating CD8$^+$ T cells were significantly lower in *MYC*-overexpressed (*MYC*^{high}) GCs and NSCLCs than in *MYC*^{low} tumors (Figures 1D and 1E). By contrast, PD-1 expression by tumor-infiltrating eTreg cells was significantly higher in *MYC*^{high} GCs and NSCLCs compared with *MYC*^{low} GCs and NSCLCs (Figure 1E).

Based on this, we hypothesized that PD-1 expression by eTreg cells could be upregulated in highly glycolytic tumors. A previous report suggests that glycolysis is promoted via hypoxia in liver metastatic lesions (Dupuy et al., 2015). Paired samples from NSCLC primary lesions and liver metastatic lesions were subjected to immunohistochemistry (IHC). The expression of glycolysis-related proteins, including LDHA, PDK1, and HIF1α, was significantly higher in liver metastatic lesions compared with primary lesions (Figures 1F and S1C; Table S3). PD-1 expression by FOXP3$^+$CD4$^+$ T cells in liver metastatic lesions was also significantly higher than that in primary lesions, while PD-1 expression by CD8$^+$ T cells was decreased (Figures 1G and 1H).

LA enhances PD-1 expression by eTreg cells, but not by CD8$^+$ T cells, through MCT1

We next explored mechanisms by which eTreg cells gained higher PD-1 expression in glycolytic tumors compared with CD8$^+$ T cells. From surgically resected NSCLC samples, four tumor-infiltrating T cell subsets, PD-1$^+$ or PD-1$^-$ CD8$^+$ T cells and PD-1$^+$ or PD-1$^-$ eTreg cells, were prepared (Figure 2A). Enrichment analysis of gene expression of the four T cell subsets was performed to identify the genes that were positively associated with PD-1 expression, specifically in eTreg cells but not in CD8$^+$ T cells (Figure 2B). Among the enriched genes that were robustly expressed by PD-1$^+$ eTreg cells, we focused on *Slc16a1* encoding MCT1, a LA transporter (Figure 2C). Given that LA is the final product of tumor glycolysis, we examined whether PD-1 expression by eTreg cells could be induced by taking up LA through MCT1 (San-Millán and Brooks, 2017). Indeed, LA content was significantly higher in advanced GC samples harboring PD-1^{high} eTreg cells than those with PD-1^{low} eTreg cells (Figure 2D). The protein expression of MCT1

(E) Representative histogram plots (left) and summaries (right) classified according to *MYC* gene expression are shown.

(F) IHC scores of LDHA, PDK1, and HIF1α were compared according to the sites of lesions of advanced NSCLC patients (cohort 3).

(G and H) Multiplexed IHC were compared according to the sites of lesions of advanced NSCLC patients. Representative pictures (G) of multiplexed IHC of primary and liver metastatic lesions for the indicated markers and summaries (H) are shown. Bars, mean; ns, not significant; *p < 0.05, **p < 0.01, ***p < 0.001; unpaired (C, D, and E) or paired (F and H) two-tailed t test.

See also Figure S1 and Tables S1–S3.

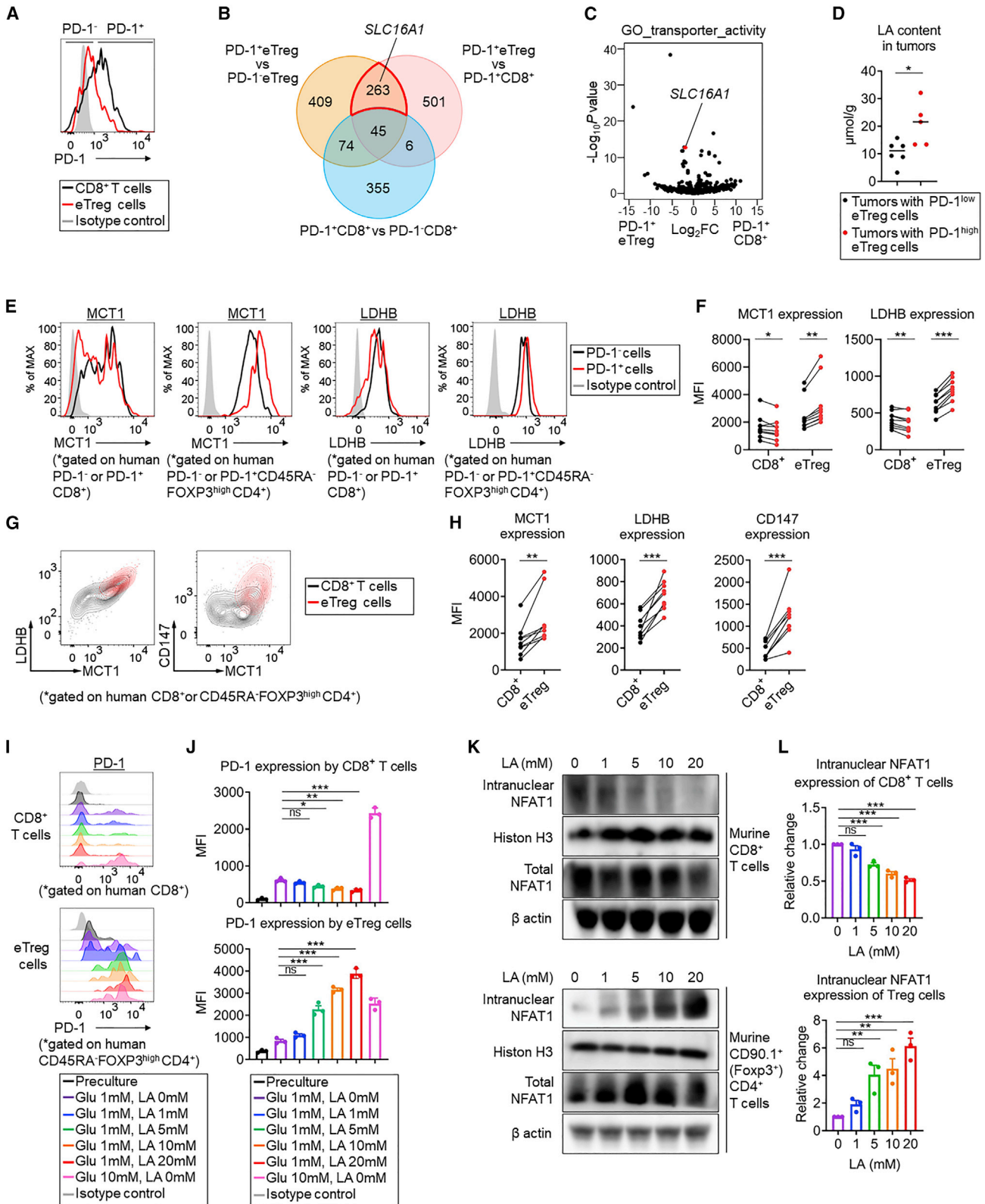**Figure 2. LA induces PD-1 expressions by eTreg cells through MCT1**

(A–C) Gene expression of PD-1^{+} and PD-1^{−} cells in each T cell subset from surgically resected NSCLC was compared. (A) Representative histogram plots of PD-1 expression are shown. (B) A Venn diagram illustrating significantly positively enriched gene numbers, which were obtained by gene expression analyses of each

by each T cell subset was examined with flow cytometry. The expression of MCT1 and LDHB, associated with LA metabolism (Chen et al., 2016), was significantly increased in PD-1$^+$ eTreg cells in the TME, while their expression was rather decreased in PD-1$^+$CD8$^+$ T cells (Figures 2E and 2F) in line with a previous report (Watson et al., 2021). Cell surface expression of MCT1 is facilitated by tight interaction with CD147 (Kirk et al., 2000), and CD147 is reportedly expressed specifically by activated human Treg cells that are identical to our eTreg cells (Solstad et al., 2011). Flow cytometric analysis of tumor-infiltrating lymphocytes from both human advanced GC samples and murine tumor models showed significantly higher protein expression of MCT1, CD147, and LDHB by eTreg cells compared with CD8$^+$ T cells (Figures 2G, 2H, and S2A–S2D). The higher expression of MCT1 and LDHB was confirmed by western blotting (Figures S2E–S2H). The analysis using chromatin immunoprecipitation sequencing (ChIP-seq) data in public datasets (Birzele et al., 2011; Schmidl et al., 2014) revealed that both *SLC16A1* and *BSG* (encoding CD147) genes harbored FOXP3 binding sites (Figure S1D). In FOXP3-overexpressing Jurkat cells, the expression of MCT1 and CD147 was significantly higher than in the control Jurkat cells (Figures S2I–S2K). These results indicate that FOXP3 directly promotes the expression of MCT1 and CD147 in eTreg cells.

We then analyzed the direct link between LA and PD-1 expression in each T cell subset, particularly eTreg cells. CD8$^+$ T cells and eTreg cells were stimulated *in vitro* with anti-CD3 and CD28 monoclonal antibodies (mAbs) under low-glucose conditions with increasing concentrations of LA. Notably, PD-1 expression by eTreg cells was significantly elevated with increasing LA concentrations. By contrast, PD-1 expression in CD8$^+$ T cells decreased in proportion to LA concentration (Figures 2I and 2J). When Treg cells take up LA from the microenvironment via MCT1, LA is metabolized into phosphoenol pyruvate (PEP) in Treg cells (Figure S3A) (Watson et al., 2021). PEP is known as a metabolic immune checkpoint and activates T cell functions (Ho et al., 2015). PEP increases calcium ion (Ca^{2+}) concentration in cytoplasm and promotes NFAT1 translocation into the nucleus. From our data, an increase of LA concentration induced significant elevation of PEP content, Ca^{2+} content, and intranuclear NFAT1 expression in Treg cells, whereas those were not elevated in CD8$^+$ T cells, when those T cells were stimulated under low-glucose conditions (Figures 2K, 2L, and S3A–S3C). Next, the impact of LA concentration on the proliferation and apoptosis of CD8$^+$ T cells and Treg cells under a low-glucose environment was assessed. CD8$^+$ T cells and

CD45RA$^-$CD25^{high}CD4$^+$ T cells (eTreg cells) were sorted from PBMCs and separately cultured. eTreg cells were vigorously proliferative and less apoptotic compared with CD8$^+$ T cells in response to increased LA under a low-glucose condition (Figures S3D–S3F). Furthermore, T cell suppression assays were performed in a low-LA or high-LA environment. The proliferation of responder (Tresp) cells was examined with carboxyfluorescein diacetate succinimidyl ester-labeled CD8$^+$ T cells cultured with/without CD45RA$^-$CD25^{high}CD4$^+$ T cells (eTreg cells). eTreg cells became more suppressive in higher-LA (low-glucose) concentration (Figure 3A).

NFAT1 positively regulates the expression of various immunological molecules including PD-1 (Müller and Rao, 2010; Oestreich et al., 2008). To directly address the relationship between PD-1 expression of each T cell subsets and MCT1, we interrogated the role of MCT1 in human T cells with pharmacological inhibition. CD8$^+$ T cells and eTreg cells from healthy individuals were treated with MCT1 inhibitor (AR-C155858, MCT1i) under low-glucose and high-LA (15 mM) conditions. PD-1 expression by eTreg cells was significantly reduced in a concentration-dependent manner, whereas MCT1i slightly increased PD-1 expression by CD8$^+$ T cells (Figures S3G and S3H). Furthermore, MCT1i treatment reduced the proliferation and suppressive activities as well as enhanced the apoptosis in eTreg cells, but not in CD8$^+$ T cells in a high-LA condition (Figures 3D and S3I–S3K). Furthermore, *Slc16a1*$^{-/-}$ mice and *Slc16a1*$^{flox/flox}$ (*Slc16a1*$^{fl/fl}$) mice were developed to confirm the results using human T cells. Since the deficiency of *Slc16a1* was lethal in the mouse, *Slc16a1*$^{+/-}$ mice were used for the following experiments. In addition, *Slc16a1*$^{fl/fl}$ mice were crossed with *Foxp3*^{Cre} mice to obtain *Foxp3*^{Cre};*Slc16a1*$^{wt/fl}$ and *Foxp3*^{Cre};*Slc16a1*$^{fl/fl}$ mice (Figure S4A). The immunological phenotypes of spleens and inguinal lymph nodes of *Foxp3*^{Cre} mice and *Foxp3*^{Cre};*Slc16a1*$^{fl/fl}$ mice were examined, and no significant differences in the frequencies and expression of immune checkpoint molecules, such as PD-1 and CTLA-4, in each T cell subset were found between *Foxp3*^{Cre} mice and *Foxp3*^{Cre};*Slc16a1*$^{fl/fl}$ mice (Figures S4B–S4E). CD8$^+$ T cells and Treg cells with genetic ablation of *Slc16a1* were stimulated with anti-CD3 and CD28 mAbs under low-glucose and high-LA (15 mM) conditions. PD-1 expression by CD8$^+$ T cells from *Slc16a1*$^{+/-}$ mice was significantly higher than in wild-type mice (Figure S4F). In sharp contrast, PD-1 expression by Treg cells was robustly inhibited by genetic ablation of *Slc16a1* (Figure S4G). We next examined the correlation between MCT1 expression and the suppressive activities of Treg cells under high-LA conditions. Under low-

T cell subset in the TME is shown. (C) Volcano plots analyzing enriched differential genes between PD-1$^+$ eTreg cells and PD-1$^+$ CD8$^+$ T cells in the TME are shown.

(D–H) TILs were collected from nine patients with advanced GC. (D) LA content was extracted from advanced GC samples and compared according to PD-1 expression by tumor-infiltrating eTreg cells (PD-1 positivity for ≥40% of eTreg cells or not). (E and F) Representative histogram plots (E) and summaries (F) are shown. (G and H) Representative contour plots (G) and summaries (H) are shown.

(I and J) CD8$^+$ T cells and eTreg cells from human healthy individuals were stimulated with the indicated concentration of glucose and LA for 24h (N = 3). Representative histogram plots (I) and summaries (J) are shown.

(K and L) CD8$^+$ T cells or CD90.1$^+$ (Foxp3$^+$) CD4$^+$ T cells from the spleen of *Foxp3*$^{Thy1.1}$ mice were stimulated under low-glucose (1 mM) condition with the indicated concentration of LA for 24 h. The total and intranuclear protein expression of NFAT1 were examined by western blotting. Representative blots of total and intranuclear NFAT1 from three independent experiments are shown (K). Summaries of quantified intranuclear NFAT1 (NFAT1/Histon H3) expression in each T cell subset relative to the expression when each T cell subset was cultured without LA are shown (N = 3) (L). Data shown as mean ± SEM; ns, not significant; *p < 0.05, **p < 0.01, ***p < 0.001; unpaired (D) or paired (F and H) two-tailed t test, and one-way ANOVA with Bonferroni's multiple comparisons test (J and L).
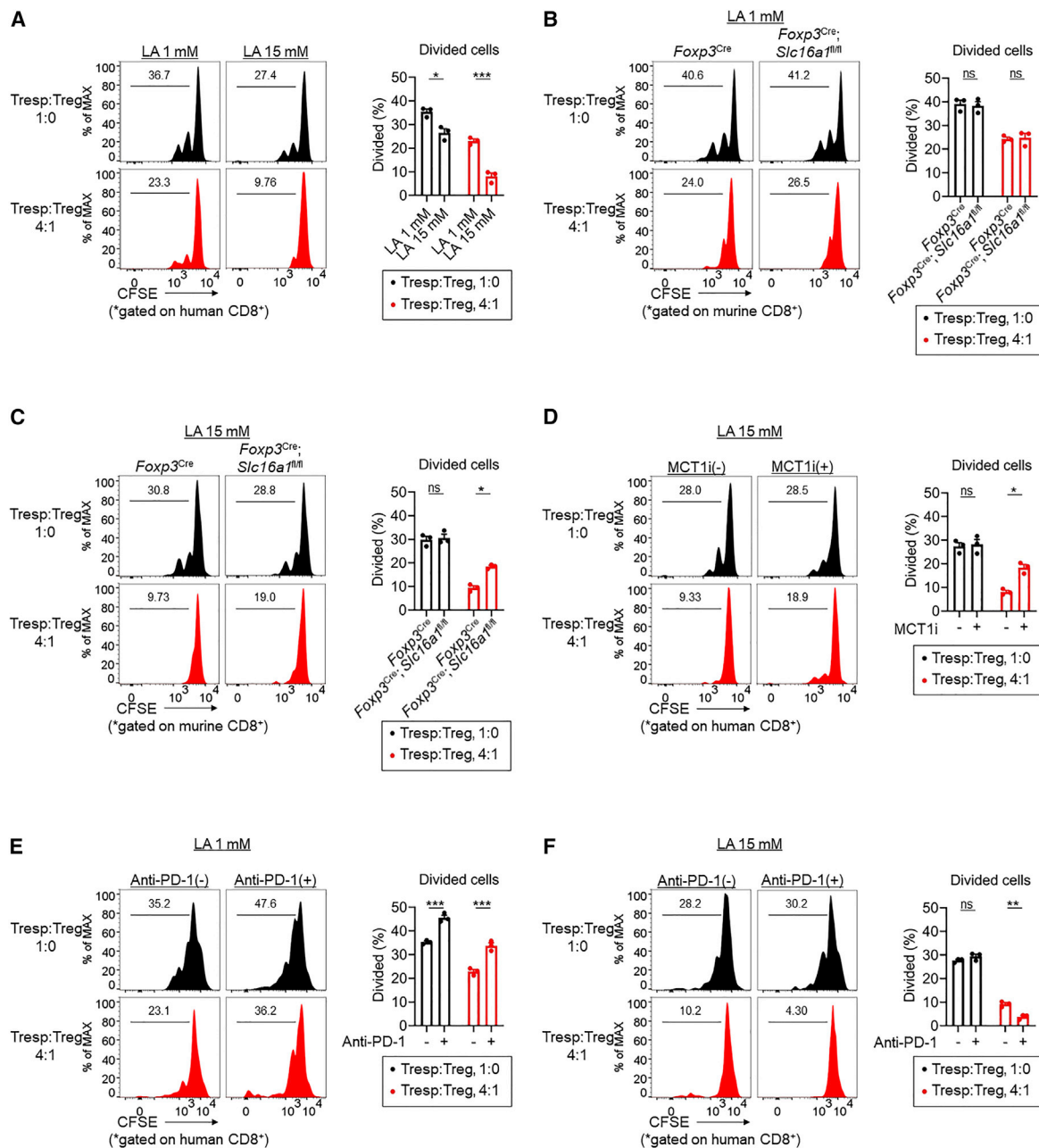See also Figures S2, S3, S4, and S5.

Figure 3. MCT1 expression by Treg cells is important for maintaining suppressive activities under a high-LA environment

(A) Suppression assays with human T cells under low-glucose (1 mM) and low-LA (1 mM) or high-LA (15 mM) condition were performed. Representative histograms (left) and summaries (right) of suppressive function under low-LA or high-LA conditions are shown (N = 3).

(B and C) Suppression assays with splenocytes of *Foxp3*^Cre or *Foxp3*^Cre;*Slc16a1*^fl/fl mice under low-glucose (1 mM) and low-LA (1 mM) (B) or high-LA (15 mM) (C) conditions were performed. Representative histograms (left) and summaries (right) of suppressive function in low-LA (B) or high-LA (C) conditions are shown (N = 3).

(D) Suppression assays with human T cells under low-glucose (1 mM) and low-LA (1 mM) or high-LA (15 mM) conditions with or without 100 nM of AR-C155858 were performed. Representative histograms (left) and summaries (right) of suppressive function are shown (N = 3).

(E and F) Suppression assays with human T cells under low-glucose (1 mM) and low-LA (1 mM) (E) or high-LA (15 mM) (F) conditions with or without anti-PD-1 mAbs were performed. Representative histograms (left) and summaries (right) of suppressive function are shown in low-LA (E) or high-LA (F) conditions (N = 3).

Data shown as mean ± SEM; ns, not significant; *p < 0.05, **p < 0.01, ***p < 0.001 unpaired two-tailed t test.
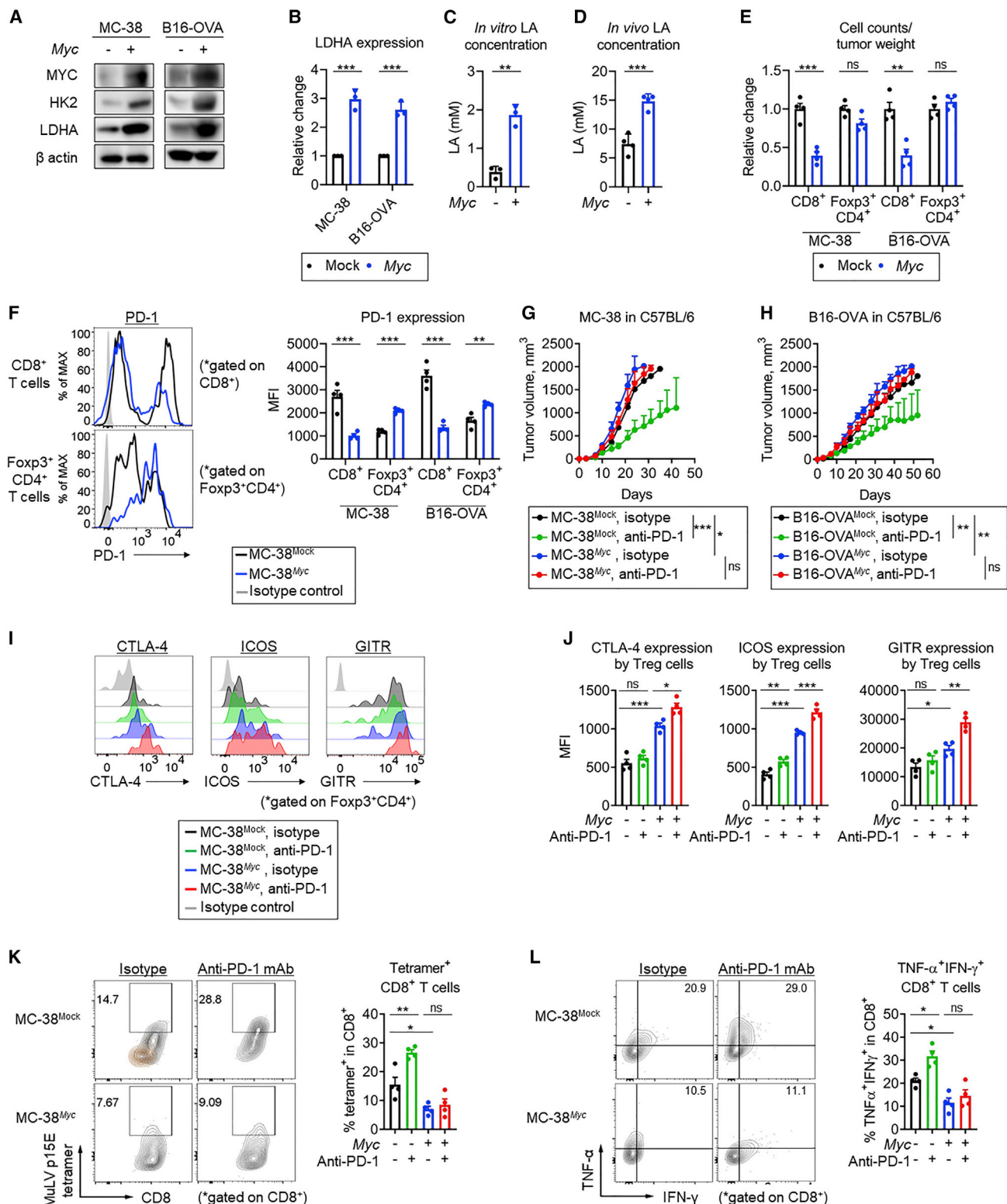
See also Figure S5.

Figure 4. MYC expression by tumor cells promotes glycolysis and leads to resistance to PD-1 blockade

(A and B) Mock and *Myc* were retrovirally transduced into MC-38 and B16-OVA cells. (A) Representative immune blots from three independent experiments are shown. (B) Summaries of quantified LDHA (LDHA/β-actin) expression by *Myc*-overexpressing cell lines relative to the expression in mock cell lines are shown (N = 3).

(legend continued on next page)

glucose and high-LA conditions, genetic ablation of *Slc16a1* in Treg cells reduced suppressive activities, but not under low-LA (normal glucose) conditions (Figures 3B and 3C). Taken together, PD-1 expression by eTreg cells is upregulated by taking up LA through MCT1, the expression of which is controlled by FOXP3, under a low-glucose and high-LA environment, although PD-1 expression by CD8$^+$ T cells shows an inverse trend.

PD-1 blockade enhances immunosuppressive activities of eTreg cells in a high-LA environment

We next addressed whether PD-1 blockade could enhance the suppressive function of eTreg cells under low-glucose and high-LA conditions. A higher concentration of LA gradually reduced the enhanced IFN-γ production of CD8$^+$ T cells by PD-1 blockade (Figure S5A). By contrast, treatment with anti-PD-1 mAbs at a higher concentration of LA enhanced suppressive activities of eTreg cells (Figures S5B–S5D).

Furthermore, suppression assays were performed under low-LA or high-LA conditions. The proliferation of Tresp cells was increased by adding anti-PD-1 mAbs in a low-LA but not in a high-LA environment (Figures 3E and 3F). When Tresp cells were cocultured with eTreg cells in a low-LA environment, Tresp cells were preferentially activated by anti-PD-1 mAbs, while eTreg cell suppression was comparable (Figure 3E). By contrast, when Tresp cells were cocultured with eTreg cells in a high-LA environment, eTreg cells augmented their suppressive activities, and the proliferation of Tresp cells was severely impaired by PD-1 blockade, suggesting the preferential activation of PD-1$^+$ eTreg cells (Figure 3F). Thus, PD-1 blockade can enhance activities of eTreg cells under a low-glucose high-LA environment, leading to a far stronger suppression to effector function of CD8$^+$ T cells, implying the direct link between high-LA-induced PD-1^{high} eTreg cells and the failure of PD-1 blockade therapy, and in some cases, hyperprogressive disease.

MYC expression regulates the balance of PD-1 expression by T cell populations by governing glycolytic activities and creating a high-LA TME

The clinical sample data with *MYC*^{high} tumors (Figures 1D and 1E) prompted us to evaluate the impact of tumoral MYC expression on PD-1 expression by T cells in the TME using animal models. We established *Myc*-overexpressing MC-38 (a murine colon carci-

noma cell line: MC-38^{Myc}) and B16-OVA (murine melanoma cell line: B16-OVA^{Myc}) (Figure 4A). The expression of hexokinase 2 and LDHA, key regulators of glycolysis, was higher in *Myc*-over-expressing cell lines than in mock cell lines (MC-38^{Mock} and B16-OVA^{Mock}) (Figure 4A and 4B). Accordingly, *Myc*-overexpressing cell lines produced significantly higher amounts of LA *in vitro* and *in vivo* compared with mock cell lines (Figures 4C and 4D). MC-38^{Myc} tumors exhibited more rapid growth than MC-38^{Mock} tumors in both immunocompromised and immunocompetent mice (Figures 4G and S6A). Accordingly, the number (counts/tumor weight) of CD8$^+$ T cells was significantly lower in MC-38^{Myc} tumors compared with MC-38^{Mock} tumors, although the number of Treg cells was comparable (Figure 4E). Significantly higher PD-1 expression by Treg cells was detected in MC-38^{Myc} tumors compared with MC-38^{Mock} tumors, although PD-1 expression by CD8$^+$ T cells was significantly lower in MC-38^{Myc} tumors than MC-38^{Mock} tumors (Figure 4F). Antitumor effects of anti-PD-1 mAbs were significantly impaired in MC-38^{Myc} tumors (Figure 4G). Similar results were observed in the B16-OVA model (Figures 4E, 4F, and 4H).

In MC-38^{Myc} tumors, anti-PD-1 mAb treatment significantly enhanced the expression of activation markers (CTLA-4, ICOS, and GITR) and proliferation (detected by Ki-67 expression) of Treg cells, while the enhancement of function and proliferation by Treg cells was not observed in MC-38^{Mock} tumors after anti-PD-1 mAb treatment (Figures 4I, 4J, and S5E). Antigen-presenting cells (APCs) are an important target of Treg cells (Bauer et al., 2014; Maeda et al., 2014; Qureshi et al., 2011; Wing et al., 2008). The maturation of APCs in the TME was dampened by anti-PD-1 mAb treatment in MC-38^{Myc} tumors (Figures S5F and S5G). The frequencies of MuLV-15E tetramer$^+$CD8$^+$ T cells and TNF-α^+IFN-γ^+ CD8$^+$ T cells in the TME were not increased by anti-PD-1 mAbs in MC-38^{Myc} tumors (Figures 4K and 4L). Thus, abundant LA in the TME of *Myc*-overexpressing tumors increases PD-1 expression especially by Treg cells, resulting in treatment resistance caused by enhanced suppressive activities of Treg cells upon PD-1 blockade.

Intrahepatic tumors enhance glycolysis and promote PD-1 expression by Treg cells in the TME

The clinical sample data (Figures 1G and 1H) also indicated that PD-1 expression by eTreg cells was predominantly induced in liver metastatic tumors. C57BL/6 mice were inoculated with MC-38 or B16-OVA cells subcutaneously or directly into the

(C) LA concentration in the culture supernatants is shown. MC-38^{Mock} and MC-38^{Myc} cell lines were cultured with RPMI medium containing 10% FBS. The concentration of LA was examined 72 h later (N = 3).
(D–F) MC-38^{Mock}, MC-38^{Myc}, B16-OVA^{Mock}, or B16-OVA^{Myc} cells (1 × 10^6) were injected subcutaneously into wild-type C57BL/6 mice on day 0. Tumor interstitial fluids and TILs were extracted from each tumor on day 15. (D) The total amount of LA in the interstitial fluids of the MC-38^{Mock} and MC-38^{Myc} tumors was evaluated (N = 4 per group). (E and F) TILs collected on day 15 were subjected to flow cytometry (FCM). The number of CD8$^+$ T cells and Foxp3$^+$CD4$^+$ T cells in the TME (counts per tumor weight) (E) and the expression of PD-1 by CD8$^+$ T cells and Foxp3$^+$CD4$^+$ T cells in the TME (F) were examined (N = 4 per group). Representative histograms (F) (left) and MFI summaries (F) (right) are shown.
(G and H) MC-38^{Mock} or MC-38^{Myc} cells (1 × 10^6) (G) and B16-OVA^{Mock} or B16-OVA^{Myc} cells (1 × 10^6) (H) were injected subcutaneously into wild-type C57BL/6 mice on day 0, and anti-PD-1 mAbs or control mAbs were administered on days 8, 11, and 14 (N = 6 per group). The tumor growth curves of the indicated groups are shown.
(I–L) MC-38^{Mock} or MC-38^{Myc} cells (1 × 10^6) were injected subcutaneously into wild-type C57BL/6 mice on day 0, and anti-PD-1 mAbs or control mAbs were administered on days 8, 11 and 14 (N = 4 per group). TILs were extracted from each tumor on day 15 and subjected to FCM. Representative histograms (I) and MFI summaries (J) are shown. (K) MC-38 antigen-specific CD8$^+$ T cells were detected by MuLV p15E/H-2Kb tetramers (N = 4 per group). Representative contour plots (left) and summaries (right) are shown. β-Galactosidase/H-2Kb tetramer staining served as a control (brown-colored contour plots). (L) Cytokine production by CD8+ T cells in the TME was examined. Representative contour plots (left) and summaries (right) are shown. Data shown as mean ± SEM; ns, not significant; *p < 0.05, **p < 0.01, ***p < 0.001; paired (B) or unpaired (C, D, E, and F) two-tailed t test, two-way ANOVA with Tukey's multiple comparisons test (G and H), and one-way ANOVA with Tukey's multiple comparisons test (J, K, and L).
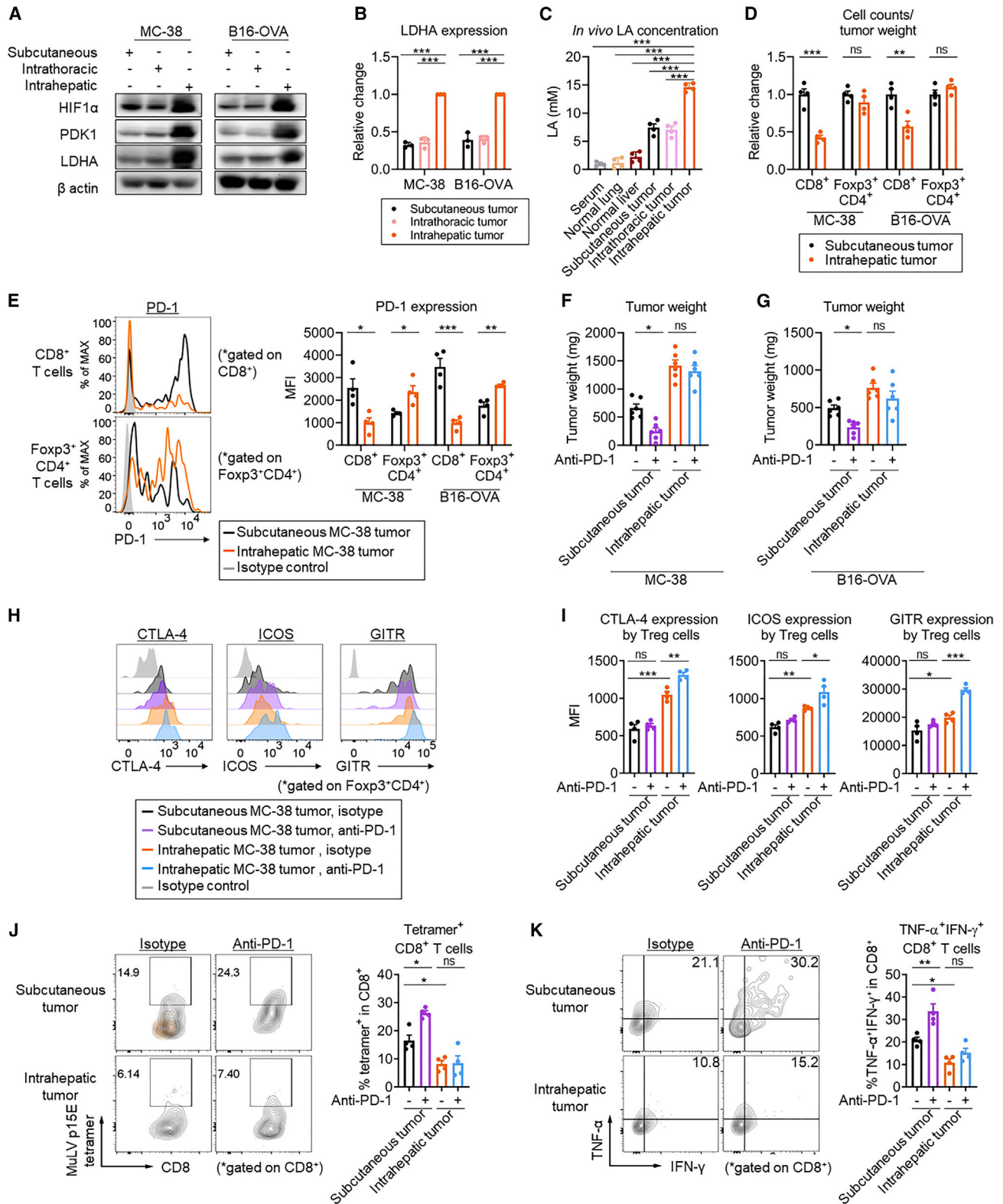
Figure 5. Intrahepatic tumors induce the hypoxic microenvironment and dampen the efficacy of PD-1 blockade

(A and B) MC-38 or B16-OVA cells (1 × 10^6) were injected into the indicated organs of wild-type C57BL/6 mice on day 0 (N = 3). Protein was extracted from the tumors on day 15. The protein expression of HIF1α, PDK1, and LDHA in tumors from indicated organs was examined by western blotting. (A) Representative blots

lung or the liver. Immuno-blotting assays revealed that intrahepatic tumors highly expressed PDK1 and LDHA via HIF1α (Figures 5A and 5B). LA concentration was significantly high in tissue interstitial fluids from intrahepatic tumors (Figure 5C). Similar to MYC-overexpressing tumors, the number and PD-1 expression of CD8+ T cells was significantly reduced in intrahepatic tumors, while PD-1 expression by Treg cells was significantly enhanced (Figures 5D and 5E). Anti-PD-1 mAb treatment did not exhibit antitumor effect against intrahepatic tumors (Figures 5F and 5G), rather activating Treg cells in intrahepatic tumors (Figures 5H, 5I, and S5H) and dampening the maturation of APCs (Figures S5I and S5J). Accordingly, tumor-reactive and/or activated CD8+ T cells were not augmented by anti-PD-1 mAbs in intrahepatic tumors (Figures 5J and 5K). Together, abundant LA in the intrahepatic TME induces PD-1 expression by Treg cells, leading to the resistance to anti-PD-1 mAb treatment.

Resistance of Myc-overexpressing tumors to PD-1 blockade is overcome by inhibiting the LA metabolism of Treg cells

We addressed whether targeting LDHA of tumor cells or MCT1 of Treg cells in the TME could recover the efficacy of anti-PD-1 mAbs in MC-38^{Myc} tumors. We generated *Ldha* knocked down MC-38^{Myc} (MC-38^{Myc}-Ldha^{RNAi}) cells (Figures S6B, S6C, and S6D). Both genetic and pharmacological (GSK2837808A, LDHi) inhibition of LDHA reduced LA production from tumors, reversed the balance of PD-1 expression in CD8+ T cells and Treg cells, and inhibited suppressive function of Treg cells, resulting in significant improvement of the efficacy of anti-PD-1 mAbs (Figures 6A–6H, S6F, S6G, and S7A–S7D). In addition, genetic and pharmacological (MCT1i) inhibition of MCT1 of Treg cells reduced the frequency of Treg cells and PD-1 expression by Treg cells in the TME and increased activated CD8+ T cells, leading to a significant inhibition of tumor growth by anti-PD-1 mAbs (Figures 6I–6P and S7E–S7H). Thus, the resistance of *Myc*-overexpressing tumors to PD-1 blockade could be overcome by targeting LDHA in tumors or MCT1 of Treg cells.

Efficacy of PD-1 blockade in intrahepatic tumors is recovered by targeting LA metabolism of Treg cells

Next, we tested whether targeting LDHA of tumor cells or MCT1 of Treg cells in the TME could augment the efficacy of anti-PD-1 mAbs in intrahepatic tumors. Similar to *Myc*-overexpressing tumors, both genetic and pharmacological inhibition of LDHA reduced LA amount from intrahepatic tumors (Figures S6E and S6H), reversed the balance of PD-1 expression by T cells, and inhibited suppressive function of Treg cells, resulting in improved efficacy of anti-PD-1 mAbs (Figures 7A–7H and S8A–S8D). In addition, genetic and pharmacological inhibition of MCT1 of Treg cells decreased the frequency of Treg cells and PD-1 expression by Treg cells and increased activated CD8+ T cells in the intrahepatic TME, thereby significantly augmenting the antitumor efficacy of anti-PD-1 mAbs (Figures 7I–7P and S8E–S8H). Thus, the antitumor effect of anti-PD-1 mAbs is recovered via inhibiting LDHA in tumors or MCT1 of Treg cells in intrahepatic tumors.

High expression of glycolysis-related molecules predicts the efficacy of PD-1 blockade in clinical cohorts

The predictive impacts of LDHA and MYC expression in patients who received PD-1 blockade therapy were examined. GC, NSCLC, and malignant melanoma patients who received PD-1 blockade were examined. Patients with high expression of LDHA or MYC exhibited a short progression-free survival (PFS) (Figures 8A, 8B, and S1C). GC patients with *MYC* amplification had a significantly shorter PFS than those without *MYC* amplification (Figure 8C). GC and NSCLC patients with liver metastasis who received PD-1 blockade therapy showed a significantly shorter PFS than those without liver metastasis (Figure 8D). Altogether, *MYC* amplification and liver metastasis are associated with resistance to ICB.

DISCUSSION

Given the limited clinical impacts of ICB therapy, developing biomarkers to stratify responders is essential for improving the clinical efficacy as immune precision medicine. We have revealed that PD-1expression by eTreg cells in the TME is associated with treatment resistance and, in some cases, hyperprogression after PD-1 blockade therapies (Kamada et al., 2019; Kumagai et al., 2020a). In Treg cells, the PD-L1–PD-1 axis inhibited the phosphorylation of ZAP70 and AKT through phosphorylation of SHP2, as observed in CD8+ T cells (Kamada et al., 2019; Kumagai et al., 2020a). Therefore, the ligation of PD-L1 to PD-1 on Treg cells dampens the suppressive activities of PD-1^{high} Treg cells. These PD-1^{high} Treg cells became more strongly suppressive through releasing the inhibition of TCR and CD28 signals by PD-L1–PD-1 axis.

---

of western blotting are shown. (B) Summary of quantified LDHA (LDHA/β-actin) expression in tumors from indicated organs relative to intrahepatic tumors is shown.

(C) MC-38 cells (1 × 10⁶) were injected into subcutaneous areas, lungs, or livers of wild-type C57BL/6 mice on day 0. Serum and interstitial fluids of normal lungs, normal livers, and each tumor were extracted on day 15 and LA concentrations of each specimen were examined (N = 4 per group).

(D and E) MC-38 (1 × 10⁶) were injected subcutaneously or into livers of wild-type C57BL/6 mice on day 0. TILs were extracted from each tumor on day 15 and subjected to FCM. The number of CD8+ and Foxp3+CD4+ T cells in the TME (counts per tumor weight) (D) and the expression of PD-1 by CD8+ T cells and Foxp3+CD4+ T cells in the TME (E) was examined (N = 4 per group). Representative histograms (E) (left) and MFI summaries (E) (right) are shown.

(F and G) MC-38 cells (1 × 10⁶) (F) or B16-OVA cells (1 × 10⁶) (G) were injected subcutaneously or into livers of C57BL/6 mice on day 0, and anti-PD-1 mAbs or control mAbs were administered on days 8, 11, and 14 (N = 6 per group). The tumor weights of the indicated groups on day 17 are shown.

(H–K) MC-38 cells (1 × 10⁶) were injected subcutaneously or into livers of wild-type C57BL/6 mice on day 0, and anti-PD-1 mAbs or control mAbs were administered on days 8, 11, and 14 (N = 4 per group). TILs were extracted from each tumor on day 15 and subjected to FCM. The expression of activation markers by Treg cells was examined. Representative histograms (H) and MFI summaries (I) are shown. (J) MC-38 antigen-specific CD8+ T cells were detected by MuLV p15E/H-2Kb tetramers (N = 4 per group). Representative contour plots (left) and summaries (right) are shown. β-Galactosidase/H-2Kb tetramer staining served as a control (brown-colored contour plots). (K) Cytokine production (IFNγ) by CD8+ T cells in the TME was examined. Representative contour plots (left) and summaries (right) are shown. Data shown as mean ± SEM; ns, not significant; *p < 0.05, **p < 0.01, ***p < 0.001; one-way ANOVA with Bonferroni's (B and C) or Tukey's (I, J, and K) multiple comparisons test, and unpaired two-tailed t test (D, E, F, and G).
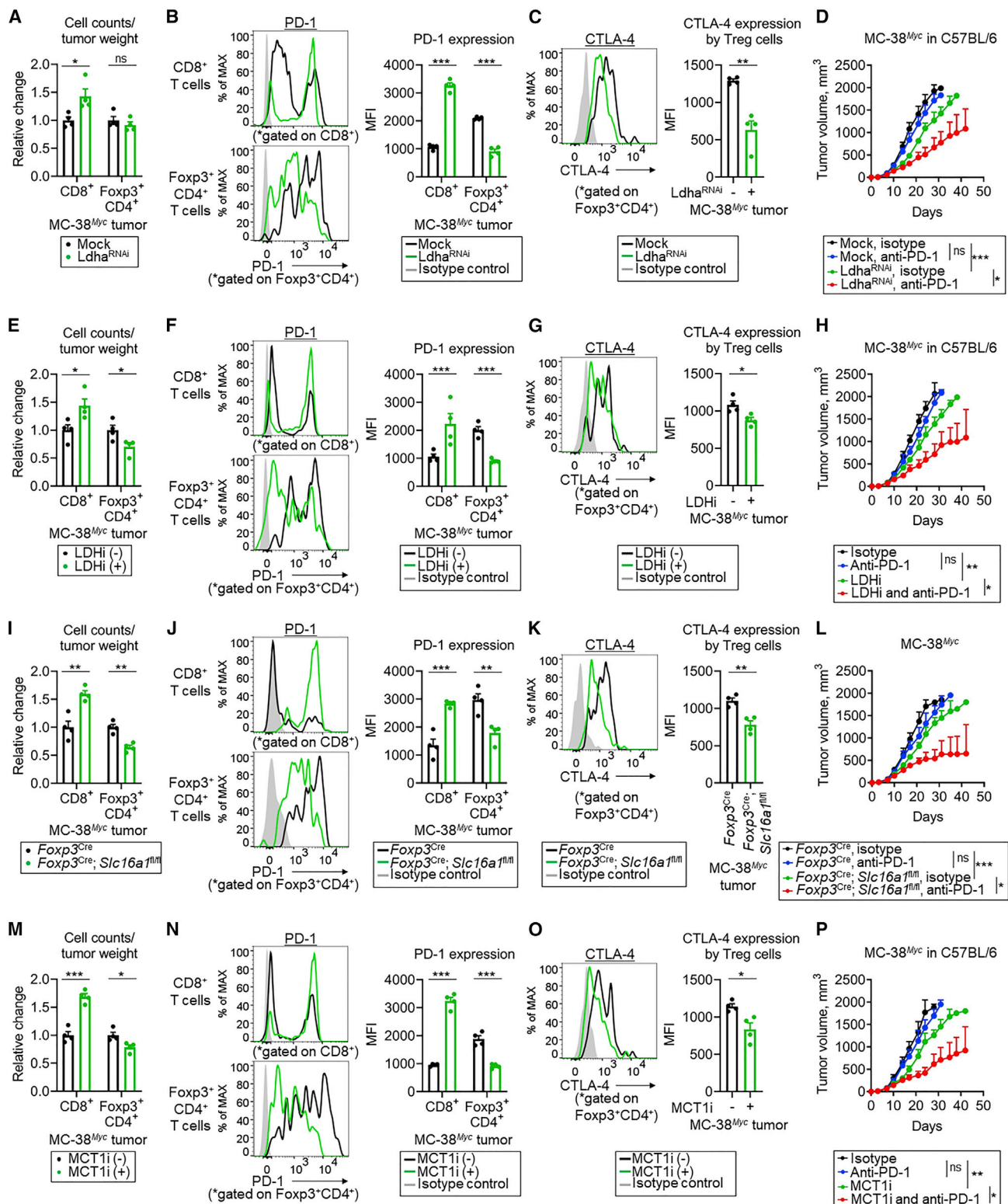
Figure 6. The resistance of MYC-overexpressingd tumors to PD-1 blockade is overcome by inhibiting the LA metabolism of Treg cells

(A–D) Mock or Ldha^{RNAi} were lentivirally transduced into MC-38^{Myc} cells. MC-38^{Myc}-Mock or MC-38^{Myc}-Ldha^{RNAi} cells (1 × 10^6) were injected subcutaneously into wild-type C57BL/6 mice on day 0. TILs were extracted from each tumor and subjected to FCM on day15. (A) The number of CD8$^+$ and Foxp3$^+$CD4$^+$ T cells in the TME (counts per tumor weight) were examined with FCM (N = 4 per group). (B) Representative histograms (left) and summaries (right) of PD-1 expression by CD8$^+$ and Foxp3$^+$CD4$^+$ T cells in the TME are shown (N = 4 per group). (C) Representative histograms (left) and summary (right) of CTLA-4 expression by

LA produced by tumor cells contributes to immune escape through inhibiting effector T cells; the highly glycolytic state of tumors is related to resistance to PD-1 blockade therapy (Brand et al., 2016; Renner et al., 2019). LA derived from glycolysis by tumor cells reduces the antitumor activity of CD8$^+$ T cells and natural killer cells (Calcinotto et al., 2012; Pilon-Thomas et al., 2016). It has been reported that Treg cells upregulate pathways involved in the LA metabolism and adapt to high-LA conditions. Deletion of MCT1 in Treg cells uncovers an important role of lactate uptake in tumor-infiltrating Treg cells with reduced tumor growth and an increased response to immunotherapy, but not in peripheral Treg cells (Watson et al., 2021). In addition, CTLA-4 blockade promotes immune cell infiltration and metabolic fitness, especially in glycolysis-low tumors, and the effect of CTLA-4 blockade to promote Treg cell destabilization depends on glycolysis and CD28 signaling of Treg cells (Zappasodi et al., 2021).

Our data illustrate that LA induced PD-1 expression in eTreg cells but repressed PD-1 expression in CD8$^+$ T cells. A higher concentration of LA increased the amount of intracellular Ca^{2+} and intranuclear NFAT in Treg cells, but not in CD8$^+$ T cells. It has been shown that FOXP3 upregulates suppressive markers, including CD25 and CTLA-4, through cooperation with NFAT (Wu et al., 2006). As a result, suppressive molecules that are associated with Treg cell functions were also highly expressed by eTreg cells, depending on the concentration of LA. A recent report suggested that lipid signaling enforces PD-1 expression by Treg cells in the TME (Lim et al., 2021). Yet, it is also possible that this lipid signaling may induce PD-1 expression by CD8$^+$ cells, because PD-1^{high} CD8$^+$ T cells in the TME reportedly utilize fatty acids (Thommen et al., 2018). Therefore, induction of PD-1 expression peculiar to Treg cells by higher-LA concentration may play a more essential role, particularly in PD-1 blockade therapy. Manufacturing effecter T cells equipped with the metabolic adaptation machinery, which enable the augmentation of the metabolic fitness of effector T cells, could be a novel treatment strategy for cell therapy.

In metabolic aspects, MYC directly targets most of the genes encoding glycolysis-related enzymes (Dang et al., 2006; Guo et al., 2000; Kim and Dang, 2006). In addition to these cell-intrinsic roles, MYC expression changes the TME to escape from antitumor immune responses; MYC increases expression of immune checkpoint molecules such as PD-L1 and CD47 (Casey et al., 2016) and downregulates expression of chemokines that recruit effector T cells (Topper et al., 2017). Upregulation of MYC causes an influx of inflammatory cells, such as neutrophils and macrophages, into the TME, which impair effector T cell responses (Sodir et al., 2020; Xu et al., 2019). Our study revealed that MYC-overexpressing tumors accelerated glycolytic activities, produced excessive amounts of LA, and then induced PD-1 expression by Treg cells, resulting in the resistance to ICB. While it has been shown that an MYC inhibitor could possibly synergize with ICB (Han et al., 2019), one concern is the simultaneous impairment of T cell activation by the MYC inhibitor. Indeed, T cells from *Myc*-deficient mice cannot respond to TCR engagement and activate/differentiate into effector T cell phenotypes (Preston et al., 2015; Wang et al., 2011). Thus, we employed inhibitors of LDHA or MCT1 and successfully recovered the resistance to ICB in murine models. Especially, an MCT1 inhibitor, AZD3965 is now under investigation in a clinical trial and the results are awaited (NCT01791595).

Accumulating evidence shows that liver metastasis reduces the response rate and worsens the prognosis of patients who received ICB (Halabi et al., 2016; Sasaki et al., 2019a; Topalian et al., 2019). Liver tumors reportedly induce the loss of systemic tumor-specific effector T cells by activated Treg cells and/or hepatic macrophages (Lee et al., 2020; Yu et al., 2021). Immune phenotypes of paired primary and liver metastatic lesions demonstrated that liver metastatic lesions promoted PD-1 expression by

---

Foxp3$^+$CD4$^+$ T cells in the TME are shown (N = 4 per group). (D) MC-38^{Myc}-Mock or MC-38^{Myc}-Ldha^{RNAi} cells (1.0 × 10^6) were injected subcutaneously into wild-type C57BL/6 mice on day 0, and anti-PD-1 mAbs or control mAbs were administered on days 8, 11, and 14 (N = 6 per group). The tumor growth curves of the indicated groups are shown.

(E–G) MC-38^{Myc} cells (1.0 × 10^6) were injected subcutaneously into wild-type C57BL/6 mice on day 0, and GSK2837808A (6 mg/kg) was administered orally for 10 days. TILs were extracted from each tumor and subjected to FCM on day 15. (E) The number of CD8$^+$ and Foxp3$^+$CD4$^+$ T cells in the TME (counts per tumor weight) were examined (N = 4 per group). (F) Representative histograms (left) and summaries (right) of PD-1 expression by CD8$^+$ and Foxp3$^+$CD4$^+$ T cells in the TME are shown (N = 4 per group). (G) Representative histograms (left) and summary (right) of CTLA-4 expression by Foxp3$^+$CD4$^+$ T cells in the TME are shown (N = 4 per group).

(H) MC-38^{Myc} cells (1 × 10^6) were injected subcutaneously into wild-type C57BL/6 mice on day 0. The mice were treated with anti-PD-1 mAbs (intravenously, on days 8, 11, and 14) and/or GSK2837808A (6 mg/kg) (orally, for 10 days) (N = 6 per group). The tumor growth curves of the indicated groups are shown (H).

(I–K) MC-38^{Myc} cells (1 × 10^6) were injected subcutaneously into *Foxp3*^{Cre} mice or Foxp3^{Cre};*Slc16a1*$^{fl/fl}$ mice on day 0. TILs were extracted from each tumor and subjected to FCM on day 15. (I) The number of CD8$^+$ and Foxp3$^+$CD4$^+$ T cells in the TME (counts per tumor weight) were examined with FCM (N = 4 per group). (J) Representative histograms (left) and summaries (right) of PD-1 expression by CD8$^+$ and Foxp3$^+$CD4$^+$ T cells in the TME are shown (N = 4 per group). (K) Representative histograms (left) and summary (right) of CTLA-4 expression by Foxp3$^+$CD4$^+$ T cells in the TME are shown (N = 4 per group).

(L) MC-38^{Myc} cells (1 × 10^6) were injected subcutaneously into *Foxp3*^{Cre} mice or Foxp3^{Cre};*Slc16a1*$^{fl/fl}$ mice on day 0. The mice were treated with anti-PD-1 mAbs (intravenously, on days 8, 11, and 14) (N = 6 per group). The tumor growth curves of the indicated groups are shown.

(M–O) MC-38^{Myc} cells (1 × 10^6) were injected subcutaneously into wild-type C57BL/6 mice on day 0, and AR-C155858 (10 mg/kg) was intraperitoneally administered for 10 days. TILs were extracted from each tumor and subjected to FCM on day 15. (M) The number of CD8$^+$ and Foxp3$^+$CD4$^+$ T cells in the TME (counts per tumor weight) were examined (N = 4 per group). (N) Representative histograms (left) and summaries (right) of PD-1 expression by CD8$^+$ and Foxp3$^+$CD4$^+$ T cells in the TME are shown (N = 4 per group). (O) Representative histograms (left) and summary (right) of CTLA-4 expression by Foxp3$^+$CD4$^+$ T cells in the TME are shown (N = 4 per group).

(P) MC-38^{Myc} cells (1 × 10^6) were injected subcutaneously into wild-type C57BL/6 mice on day 0. The mice were treated with anti-PD-1 mAbs (intravenously, on days 8, 11, and 14) and/or AR-C155858 (10 mg/kg) (intraperitoneally, for 10 days) (N = 6 per group). The tumor growth curves of the indicated groups are shown.

Data shown as mean ± SEM; ns, not significant; *p < 0.05, **p < 0.01, ***p < 0.001; unpaired two-tailed t test (A, B, C, E, F, G, I, J, K, M, N, and O) and two-way ANOVA with Tukey's multiple comparisons test (D, H, L, and P).
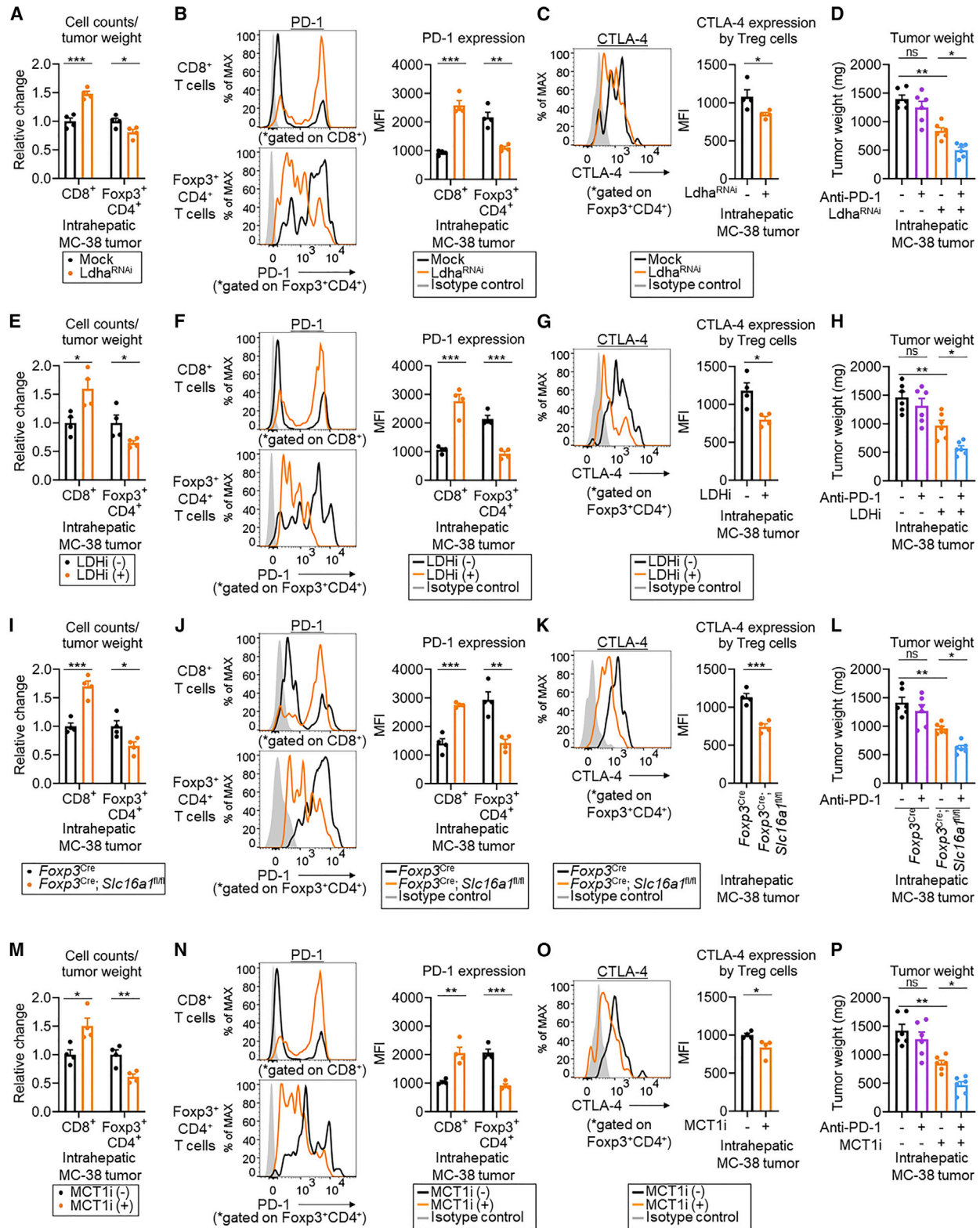
See also Figure S7.

Figure 7. The efficacy of PD-1 blockade against intrahepatic tumors is improved by targeting the LA metabolism of Treg cells

(A–D) MC-38-Mock or MC-38-Ldha^{RNAi} cells (1 × 10^6) were injected into livers of wild-type C57BL/6 mice on day 0. TILs were extracted from each tumor and subjected to FCM on day 15. (A) The numbers of CD8$^+$ and Foxp3$^+$CD4$^+$ T cells in the TME (counts per tumor weight) were examined with FCM (N = 4 per group).

Treg cells; the expression of HIF1α, PDK1, and LDHA was significantly higher in liver metastatic lesions than in other lesions, being consistent with a previous report (Dupuy et al., 2015). In addition, Treg cells highly express PD-1 in the patients infected with HCV infection (Franceschini et al., 2009). Liver receives both oxygenated and deoxygenated blood, perhaps leading to a severe hypoxic state of liver tumors compared with tumors in other organs. Our data clearly demonstrate that targeting LDHA and MCT1 could strengthen the efficacy of ICB in treating intrahepatic tumors.

In conclusion, highly glycolytic tumors deprive glucose and release excessive amounts of LA that augment PD-1 expression and suppressive activity of Treg cells, which partly contributes to the lack of efficacy of PD-1 blockade therapy. This active immunosuppressive mechanism by LA via a metabolic checkpoint peculiar to Treg cells opens a new window for developing a molecular-targeted therapy against LA as cancer immunotherapy.

STAR★METHODS

Detailed methods are provided in the online version of this paper and include the following:

- ● KEY RESOURCES TABLE
- ● RESOURCE AVAILABILITY
  - ○ Lead contact
  - ○ Material availability
  - ○ Data and code availability
- ● EXPERIMENTAL MODEL AND SUBJECT DETAILS
  - ○ Patients and samples
  - ○ Cell lines and reagents
  - ○ In vivo animal models
- ● METHOD DETAILS

- ○ Generation of Slc16a1 knocked-out and conditional knocked-out mice
- ○ RNA-seq for tumor samples
- ○ RNA-seq for TILs
- ○ Real-time reverse transcription PCR (qRT-PCR)
- ○ WES and mutational analysis
- ○ Gene expression data analysis
- ○ ChIP-seq data processing
- ○ FCM analysis
- ○ Evaluation of Ca^{2+} concentration
- ○ Apoptosis analysis
- ○ Proliferation analysis
- ○ IHC
- ○ Western blotting
- ○ Assay measuring LA concentration
- ○ LC-MS assay for PEP
- ○ T cell culture with LA
- ○ Suppression assay with murine T cells
- ○ Suppression assay with human T cells
- ● QUANTIFICATION AND STATISTICAL ANALYSIS

(B) Representative histograms (left) and summaries (right) of PD-1 expression by CD8⁺ and Foxp3⁺CD4⁺ T cells in the TME are shown (N = 4 per group). (C) Representative histograms (left) and summary (right) of CTLA-4 expression by Foxp3⁺CD4⁺ T cells in the TME are shown (N = 4 per group). (D) MC-38-Mock or MC-38-Ldha^RNAi cells (1 × 10⁶) were injected into livers of C57BL/6 mice on day 0, and anti-PD-1 mAbs or control mAbs were administered on days 8, 11, and 14 (N = 6 per group). The tumor weights of the indicated groups on day 17 are shown.
(E–G) MC-38 cells (1 × 10⁶) were injected into livers of wild-type C57BL/6 mice on day 0, and GSK2837808A (6 mg/kg) was administered orally for 10 days. TILs were extracted from each tumor and subjected to FCM on day 15. (E) The number of CD8⁺ and Foxp3⁺CD4⁺ T cells in the TME (counts per tumor weight) were examined (N = 4 per group). (F) Representative histograms (left) and summaries (right) of PD-1 expression by CD8⁺ and Foxp3⁺CD4⁺ T cells in the TME are shown (N = 4 per group). (G) Representative histograms (left) and summary (right) of CTLA-4 expression by Foxp3⁺CD4⁺ T cells in the TME are shown (N = 4 per group). (H) MC-38 cells (1 × 10⁶) were injected into livers of C57BL/6 mice on day 0. The mice were treated with anti-PD-1 mAbs (intravenously, on days 8, 11, and 14) and/or GSK2837808A (6 mg/kg) (orally, for 10 days) (N = 6 per group). The tumor weights of the indicated groups on day 17 are shown.
(I–K) MC-38 cells (1 × 10⁶) were injected into livers of *Foxp3*^Cre mice or Foxp3^Cre;*Slc16a1*^fl/fl mice on day 0. TILs were extracted from each tumor and subjected to FCM on day 15. (I) The number of CD8⁺ T cells and Foxp3⁺CD4⁺ T cells in the TME (counts per tumor weight) were examined (N = 4 per group). (J) Representative histograms (left) and summaries (right) of PD-1 expression by CD8⁺ and Foxp3⁺CD4⁺ T cells in the TME are shown (N = 4 per group). (K) Representative histograms (left) and summary (right) of CTLA-4 expression by Foxp3⁺CD4⁺ T cells in the TME are shown (N = 4 per group).
(L) MC-38 cells (1.0 × 10⁶) were injected into livers of *Foxp3*^Cre mice or Foxp3^Cre;*Slc16a1*^fl/fl mice on day 0. The mice were treated with anti-PD-1 mAbs (intravenously, on days 8, 11, and 14) (N = 6 per group). The tumor weights of the indicated groups on day 17 are shown.
(M–O) MC-38 cells (1.0 × 10⁶) were injected into livers of wild-type C57BL/6 mice on day 0, and AR-C155858 (10 mg/kg) was intraperitoneally administered for 10 days. TILs were extracted from each tumor and subjected to FCM on day 15. (M) The number of CD8⁺ and Foxp3⁺CD4⁺ T cells in the TME (counts per tumor weight) were examined (N = 4 per group). (N) Representative histograms (left) and summaries (right) of PD-1 expression by CD8⁺ and Foxp3⁺CD4⁺ T cells in the TME are shown (N = 4 per group). (O) Representative histograms (left) and summary (right) of CTLA-4 expression by Foxp3⁺CD4⁺ T cells in the TME are shown (N = 4 per group).
(P) MC-38 cells (1 × 10⁶) were injected into livers of wild-type C57BL/6 mice on day 0. The mice were treated with anti-PD-1 mAbs (intravenously, on days 8, 11, and 14) and/or AR-C155858 (10 mg/kg) (MCT1i) (intraperitoneally, for 10 days) (N = 6 per group). The tumor weights of the indicated groups on day 17 are shown.
Data shown as mean ± SEM; ns, not significant; *p < 0.05, **p < 0.01, ***p < 0.001; unpaired two-tailed t test (A, B, C, E, F, G, I, J, K, M, N, and O) and one-way ANOVA with Tukey's multiple comparisons test (D, H, L, and P).
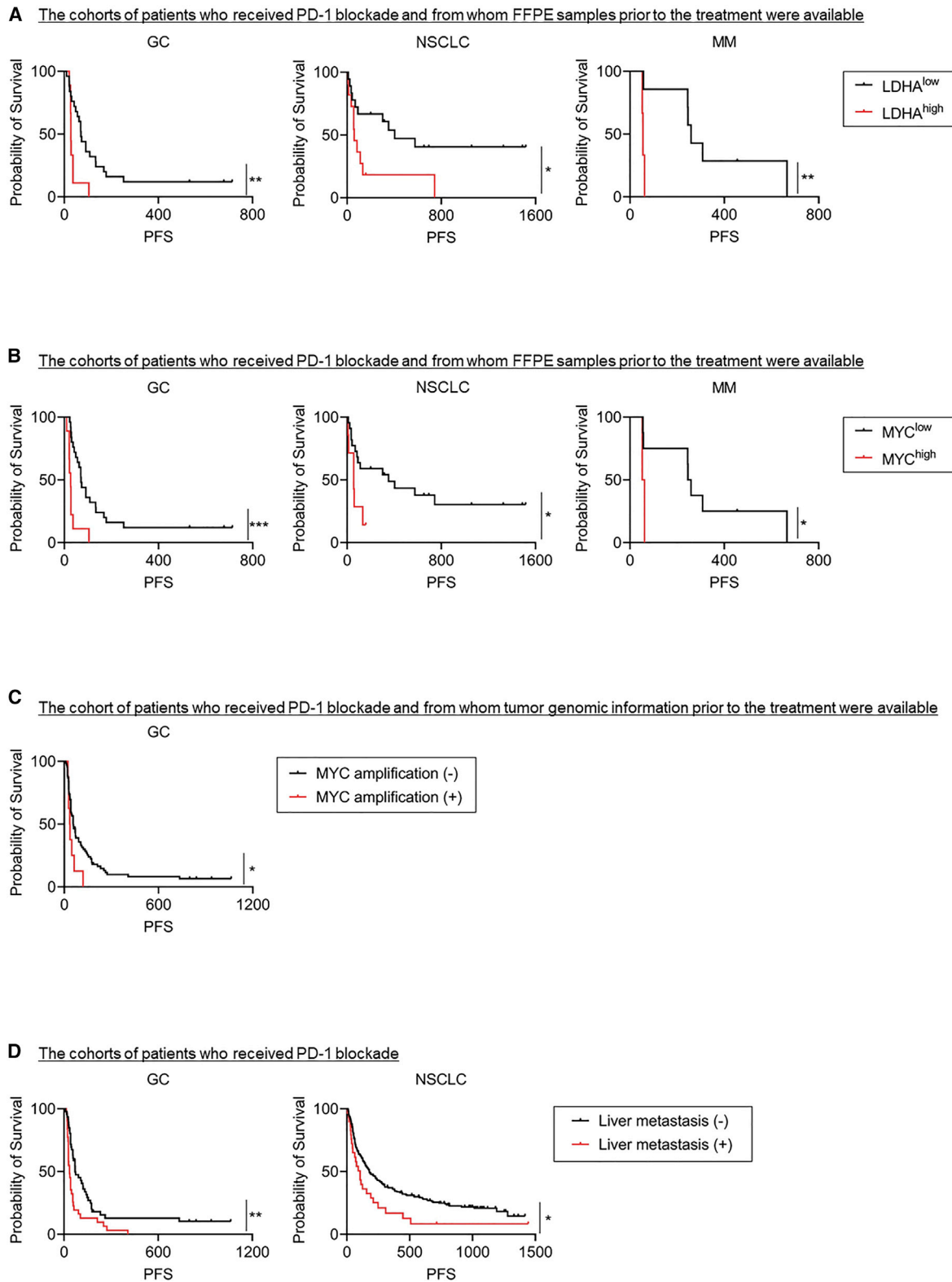See also Figure S8.

Figure 8. High expression of glycolysis-related molecules is negatively associated with the efficacy of PD-1 blockade in patients' cohorts
(A and B) Kaplan-Meier curves for PFS of patients treated with anti-PD-1 mAbs in the GC (Table S4), NSCLC (Table S5), or malignant melanoma (MM) (Table S6) cohorts in which FFPE samples before treatment were available. PFS was compared according to IHC scores of LDHA (A) or MYC (B) of tumors.

(legend continued on next page)

AUTHOR CONTRIBUTIONS

Conceptualization, S.Kumagai, S.Koyama, and H.Nishikawa; methodology, S.Kumagai, S.Koyama, K.I., Y.Togashi, and H.Nishikawa; investigation, S.Kumagai, T.Kamada⁺, G.O., D.I., G.W., T.O., H.K., K.I., T.T., T.I., Y.L., R.F., S.W., A.S., S.F., E.S., H.Nishinakamura, D.S., Y.M., Y.O., M.K., and T.U.; collection of clinical specimens and data, A.K., H.Y., K.C., T.Yoshida, Y.S., Y.Takeyasu, M.S., K.N., K.A., N.S. T.M., G.I., T.Kuwata, N.Y., Y.O., M.T., Y.Y., T.Kinoshita, T.D., and K.S.; writing – original draft, S.Kumagai, S.Koyama, and H.Nishikawa; writing – review & editing, S.Kumagai, S.Koyama, H.M., and H.Nishikawa.

DECLARATION OF INTERESTS

REFERENCES

Angelin, A., Gil-de-Gómez, L., Dahiya, S., Jiao, J., Guo, L., Levine, M.H., Wang, Z., Quinn, W.J., 3rd, Kopinski, P.K., Wang, L., et al. (2017). Foxp3 reprograms T cell metabolism to function in low-glucose, high-lactate environments. Cell Metab. *25*, 1282–1293.e7.

Bauer, C.A., Kim, E.Y., Marangoni, F., Carrizosa, E., Claudio, N.M., and Mempel, T.R. (2014). Dynamic Treg interactions with intratumoral APCs promote local CTL dysfunction. J. Clin. Invest. *124*, 2425–2440.

Birzele, F., Fauti, T., Stahl, H., Lenter, M.C., Simon, E., Knebel, D., Weith, A., Hildebrandt, T., and Mennerich, D. (2011). Next-generation insights into regulatory T cells: expression profiling and FoxP3 occupancy in Human. Nucleic Acids Res. *39*, 7946–7960.

Brand, A., Singer, K., Koehl, G.E., Kolitzus, M., Schoenhammer, G., Thiel, A., Matos, C., Bruss, C., Klobuch, S., Peter, K., et al. (2016). LDHA-Associated lactic acid production blunts tumor immunosurveillance by T and NK cells. Cell Metab. *24*, 657–671.

Calcinotto, A., Filipazzi, P., Grioni, M., Iero, M., De Milito, A., Ricupito, A., Cova, A., Canese, R., Jachetti, E., Rossetti, M., et al. (2012). Modulation of microenvironment acidity reverses anergy in human and murine tumor-infiltrating T lymphocytes. Cancer Res. *72*, 2746–2756.

Casey, S.C., Tong, L., Li, Y., Do, R., Walz, S., Fitzgerald, K.N., Gouw, A.M., Baylot, V., Gütgemann, I., Eilers, M., et al. (2016). MYC regulates the antitumor immune response through CD47 and PD-L1. Science *352*, 227–231.

Chen, Y.J., Mahieu, N.G., Huang, X., Singh, M., Crawford, P.A., Johnson, S.L., Gross, R.W., Schaefer, J., and Patti, G.J. (2016). Lactate metabolism is associated with mammalian mitochondria. Nat. Chem. Biol. *12*, 937–943.

Curiel, T.J., Coukos, G., Zou, L., Alvarez, X., Cheng, P., Mottram, P., Evdemon-Hogan, M., Conejo-Garcia, J.R., Zhang, L., Burow, M., et al. (2004). Specific recruitment of regulatory T cells in ovarian carcinoma fosters immune privilege and predicts reduced survival. Nat. Med. *10*, 942–949.

Dang, C.V., O'Donnell, K.A., Zeller, K.I., Nguyen, T., Osthus, R.C., and Li, F. (2006). The c-Myc target gene network. Semin. Cancer Biol. *16*, 253–264.

Dominguez-Villar, M., and Hafler, D.A. (2018). Regulatory T cells in autoimmune disease. Nat. Immunol. *19*, 665–673.

Dong, H., Strome, S.E., Salomao, D.R., Tamura, H., Hirano, F., Flies, D.B., Roche, P.C., Lu, J., Zhu, G., Tamada, K., et al. (2002). Tumor-associated B7-H1 promotes T-cell apoptosis: a potential mechanism of immune evasion. Nat. Med. *8*, 793–800.

Dupuy, F., Tabariès, S., Andrzejewski, S., Dong, Z., Blagih, J., Annis, M.G., Omeroglu, A., Gao, D., Leung, S., Amir, E., et al. (2015). PDK1-Dependent metabolic reprogramming dictates metastatic potential in breast cancer. Cell Metab. *22*, 577–589.

Fantin, V.R., St-Pierre, J., and Leder, P. (2006). Attenuation of LDH-A expression uncovers a link between glycolysis, mitochondrial physiology, and tumor maintenance. Cancer Cell *9*, 425–434.

(C) Kaplan-Meier curves for PFS of patients treated with anti-PD-1 mAbs in the GC cohort (Table S7) who were subjected to the evaluation of *MYC* amplification. PFS was compared according to the gene status of *MYC*.

(D) Kaplan-Meier curves for PFS of patients treated with anti-PD-1 mAbs in the GC (left; Table S7) or NSCLC (right; Table S8) cohorts. PFS of patients with liver metastasis were compared with those without liver metastasis. ns, not significant; *$p < 0.05$, **$p < 0.01$, ***$p < 0.001$ (log rank test).

See also Tables S4–S8.

Franceschini, D., Paroli, M., Francavilla, V., Videtta, M., Morrone, S., Labbadia, G., Cerino, A., Mondelli, M.U., and Barnaba, V. (2009). PD-L1 negatively regulates CD4⁺CD25⁺Foxp3⁺ Tregs by limiting STAT-5 phosphorylation in patients chronically infected with HCV. J. Clin. Invest. *119*, 551–564.

Fridman, W.H., Pages, F., Sautes-Fridman, C., and Galon, J. (2012). The immune contexture in human tumours: impact on clinical outcome. Nat. Rev. Cancer *12*, 298–306.

Gatenby, R.A., and Gillies, R.J. (2004). Why do cancers have high aerobic glycolysis? Nat. Rev. Cancer *4*, 891–899.

Guo, Q.M., Malek, R.L., Kim, S., Chiao, C., He, M., Ruffy, M., Sanka, K., Lee, N.H., Dang, C.V., and Liu, E.T. (2000). Identification of c-myc responsive genes using rat cDNA microarray. Cancer Res. *60*, 5922–5928.

Halabi, S., Kelly, W.K., Ma, H., Zhou, H., Solomon, N.C., Fizazi, K., Tangen, C.M., Rosenthal, M., Petrylak, D.P., Hussain, M., et al. (2016). Meta-analysis evaluating the impact of site of metastasis on overall survival in men with castration-resistant prostate cancer. J. Clin. Oncol. *34*, 1652–1659.

Han, H., Jain, A.D., Truica, M.I., Izquierdo-Ferrer, J., Anker, J.F., Lysy, B., Sagar, V., Luan, Y., Chalmers, Z.R., Unno, K., et al. (2019). Small-molecule MYC inhibitors suppress tumor growth and enhance immunotherapy. Cancer Cell *36*, 483–497.e5.

Hanahan, D., and Weinberg, R.A. (2011). Hallmarks of cancer: the next generation. Cell *144*, 646–674.

Ho, P.C., Bihuniak, J.D., Macintyre, A.N., Staron, M., Liu, X., Amezquita, R., Tsui, Y.C., Cui, G., Micevic, G., Perales, J.C., et al. (2015). Phosphoenolpyruvate is a metabolic checkpoint of anti-tumor T cell responses. Cell *162*, 1217–1228.

Ho, P.C., and Kaech, S.M. (2017). Reenergizing T cell anti-tumor immunity by harnessing immunometabolic checkpoints and machineries. Curr. Opin. Immunol. *46*, 38–44.

Junker, B.H., Klukas, C., and Schreiber, F. (2006). VANTED: a system for advanced data analysis and visualization in the context of biological networks. BMC Bioinformatics *7*, 109.

Kamada, T., Togashi, Y., Tay, C., Ha, D., Sasaki, A., Nakamura, Y., Sato, E., Fukuoka, S., Tada, Y., Tanaka, A., et al. (2019). PD-1⁺ regulatory T cells amplified by PD-1 blockade promote hyperprogression of cancer. Proc. Natl. Acad. Sci. U S A. *116*, 9999–10008.

Kim, D., Pertea, G., Trapnell, C., Pimentel, H., Kelley, R., and Salzberg, S.L. (2013). TopHat2: accurate alignment of transcriptomes in the presence of insertions, deletions and gene fusions. Genome Biol. *14*, R36.

Kim, J.W., and Dang, C.V. (2006). Cancer's molecular sweet tooth and the Warburg effect. Cancer Res. *66*, 8927–8930.

Kirk, P., Wilson, M.C., Heddle, C., Brown, M.H., Barclay, A.N., and Halestrap, A.P. (2000). CD147 is tightly associated with lactate transporters MCT1 and MCT4 and facilitates their cell surface expression. The EMBO J. *19*, 3896–3904.

Koyama, S., Akbay, E.A., Li, Y.Y., Aref, A.R., Skoulidis, F., Herter-Sprie, G.S., Buczkowski, K.A., Liu, Y., Awad, M.M., Denning, W.L., et al. (2016). STK11/LKB1 deficiency promotes neutrophil recruitment and proinflammatory cytokine production to suppress T-cell activity in the lung tumor microenvironment. Cancer Res. *76*, 999–1008.

Kumagai, S., Koyama, S., and Nishikawa, H. (2021). Antitumour immunity regulated by aberrant ERBB family signalling. Nat. Rev. Cancer *21*, 181–197.

Kumagai, S., Togashi, Y., Kamada, T., Sugiyama, E., Nishinakamura, H., Takeuchi, Y., Vitaly, K., Itahashi, K., Maeda, Y., Matsui, S., et al. (2020a). The PD-1 expression balance between effector and regulatory T cells predicts the clinical efficacy of PD-1 blockade therapies. Nat. Immunol. *21*, 1346–1358.

Kumagai, S., Togashi, Y., Sakai, C., Kawazoe, A., Kawazu, M., Ueno, T., Sato, E., Kuwata, T., Kinoshita, T., Yamamoto, M., et al. (2020b). An oncogenic alteration creates a microenvironment that promotes tumor progression by conferring a metabolic advantage to regulatory T cells. Immunity *53*, 187–203.e8.

Lee, J.C., Mehdizadeh, S., Smith, J., Young, A., Mufazalov, I.A., Mowery, C.T., Daud, A., and Bluestone, J.A. (2020). Regulatory T cell control of systemic immunity and immunotherapy response in liver metastasis. Sci. Immunol. *5*. https://doi.org/10.1126/sciimmunol.aba0759.

Li, H., and Durbin, R. (2009). Fast and accurate short read alignment with Burrows-Wheeler transform. Bioinformatics *25*, 1754–1760.

Li, H., Handsaker, B., Wysoker, A., Fennell, T., Ruan, J., Homer, N., Marth, G., Abecasis, G., and Durbin, R. (2009). The sequence alignment/map format and SAMtools. Bioinformatics *25*, 2078–2079.

Li, M.O., and Rudensky, A.Y. (2016). T cell receptor signalling in the control of regulatory T cell differentiation and function. Nat. Rev. Immunol. *16*, 220–233.

Lim, S.A., Wei, J., Nguyen, T.M., Shi, H., Su, W., Palacios, G., Dhungana, Y., Chapman, N.M., Long, L., Saravia, J., et al. (2021). Lipid signalling enforces functional specialization of T(reg) cells in tumours. Nature *591*, 306–311.

Müller, M.R., and Rao, A. (2010). NFAT, immunity and cancer: a transcription factor comes of age. Nat. Rev. Immunol. *10*, 645–656.

Maeda, Y., Nishikawa, H., Sugiyama, D., Ha, D., Hamaguchi, M., Saito, T., Nishioka, M., Wing, J.B., Adeegbe, D., Katayama, I., et al. (2014). Detection of self-reactive CD8⁺ T cells with an anergic phenotype in healthy individuals. Science *346*, 1536–1540.

Miyara, M., Yoshioka, Y., Kitoh, A., Shima, T., Wing, K., Niwa, A., Parizot, C., Taflin, C., Heike, T., Valeyre, D., et al. (2009). Functional delineation and differentiation dynamics of human CD4⁺ T cells expressing the FoxP3 transcription factor. Immunity *30*, 899–911.

Oestreich, K.J., Yoon, H., Ahmed, R., and Boss, J.M. (2008). NFATc1 regulates PD-1 expression upon T cell activation. J. Immunol. *181*, 4832–4839.

Pardoll, D.M. (2012). The blockade of immune checkpoints in cancer immunotherapy. Nat. Rev. Cancer *12*, 252–264.

Peng, W., Chen, J.Q., Liu, C., Malu, S., Creasy, C., Tetzlaff, M.T., Xu, C., McKenzie, J.A., Zhang, C., Liang, X., et al. (2016). Loss of PTEN promotes resistance to T cell-mediated immunotherapy. Cancer Discov. *6*, 202–216.

Pilon-Thomas, S., Kodumudi, K.N., El-Kenawi, A.E., Russell, S., Weber, A.M., Luddy, K., Damaghi, M., Wojtkowiak, J.W., Mulé, J.J., Ibrahim-Hashim, A., et al. (2016). Neutralization of tumor acidity improves antitumor responses to immunotherapy. Cancer Res. *76*, 1381–1390.

Preston, G.C., Sinclair, L.V., Kaskar, A., Hukelmann, J.L., Navarro, M.N., Ferrero, I., MacDonald, H.R., Cowling, V.H., and Cantrell, D.A. (2015). Single cell tuning of Myc expression by antigen receptor signal strength and interleukin-2 in T lymphocytes. EMBO J. *34*, 2008–2024.

Qureshi, O.S., Zheng, Y., Nakamura, K., Attridge, K., Manzotti, C., Schmidt, E.M., Baker, J., Jeffery, L.E., Kaur, S., Briggs, Z., et al. (2011). Trans-endocytosis of CD80 and CD86: a molecular basis for the cell-extrinsic function of CTLA-4. Science *332*, 600–603.

Renner, K., Bruss, C., Schnell, A., Koehl, G., Becker, H.M., Fante, M., Menevse, A.N., Kauer, N., Blazquez, R., Hacker, L., et al. (2019). Restricting glycolysis preserves T cell effector functions and augments checkpoint therapy. Cell Rep. *29*, 135–150.e9.

Robinson, M.D., McCarthy, D.J., and Smyth, G.K. (2010). edgeR: a Bioconductor package for differential expression analysis of digital gene expression data. Bioinformatics *26*, 139–140.

Rooney, M.S., Shukla, S.A., Wu, C.J., Getz, G., and Hacohen, N. (2015). Molecular and genetic properties of tumors associated with local immune cytolytic activity. Cell *160*, 48–61.

Saito, T., Nishikawa, H., Wada, H., Nagano, Y., Sugiyama, D., Atarashi, K., Maeda, Y., Hamaguchi, M., Ohkura, N., Sato, E., et al. (2016). Two FOXP3⁺CD4⁺ T cell subpopulations distinctly control the prognosis of colorectal cancers. Nat. Med. *22*, 679–684.

Sakaguchi, S., Sakaguchi, N., Asano, M., Itoh, M., and Toda, M. (1995). Immunologic self-tolerance maintained by activated T cells expressing IL-2 receptor α-chains (CD25). Breakdown of a single mechanism of self-tolerance causes various autoimmune diseases. J. Immunol. *155*, 1151–1164.

San-Millán, I., and Brooks, G.A. (2017). Reexamining cancer metabolism: lactate production for carcinogenesis could be the purpose and explanation of the Warburg effect. Carcinogenesis *38*, 119–133.

Sasaki, A., Nakamura, Y., Mishima, S., Kawazoe, A., Kuboki, Y., Bando, H., Kojima, T., Doi, T., Ohtsu, A., Yoshino, T., et al. (2019a). Predictive factors for hyperprogressive disease during nivolumab as anti-PD1 treatment in patients with advanced gastric cancer. Gastric Cancer *22*, 793–802.

Sasaki, K., Sagawa, H., Suzuki, M., Yamamoto, H., Tomita, M., Soga, T., and Ohashi, Y. (2019b). Metabolomics platform with capillary electrophoresis coupled with high-resolution mass spectrometry for plasma analysis. Anal. Chem. *91*, 1295–1301.

Sato, E., Olson, S.H., Ahn, J., Bundy, B., Nishikawa, H., Qian, F., Jungbluth, A.A., Frosina, D., Gnjatic, S., Ambrosone, C., et al. (2005). Intraepithelial CD8+ tumor-infiltrating lymphocytes and a high CD8+/regulatory T cell ratio are associated with favorable prognosis in ovarian cancer. Proc. Natl. Acad. Sci. U S A. *102*, 18538–18543.

Schmidl, C., Hansmann, L., Lassmann, T., Balwierz, P.J., Kawaji, H., Itoh, M., Kawai, J., Nagao-Sato, S., Suzuki, H., Andreesen, R., et al. (2014). The enhancer and promoter landscape of human regulatory and conventional T-cell subpopulations. Blood *123*, e68–78.

Schneider, C., Rasband, W., and Eliceiri, K. (2012). NIH Image to ImageJ: 25 years of image analysis. Nat Methods *9*, 671–675. https://doi.org/10.1038/nmeth.2089.

Sodir, N.M., Kortlever, R.M., Barthet, V.J.A., Campos, T., Pellegrinet, L., Kupczak, S., Anastasiou, P., Swigart, L.B., Soucek, L., Arends, M.J., et al. (2020). MYC instructs and maintains pancreatic adenocarcinoma phenotype. Cancer Discov. *10*, 588–607.

Solstad, T., Bains, S.J., Landskron, J., Aandahl, E.M., Thiede, B., Taskén, K., and Torgersen, K.M. (2011). CD147 (Basigin/Emmprin) identifies FoxP3+CD45RO+CTLA4+-activated human regulatory T cells. Blood *118*, 5141–5151.

Subramanian, A., Tamayo, P., Mootha, V.K., Mukherjee, S., Ebert, B.L., Gillette, M.A., Paulovich, A., Pomeroy, S.L., Golub, T.R., Lander, E.S., et al. (2005). Gene set enrichment analysis: a knowledge-based approach for interpreting genome-wide expression profiles. Proc. Natl. Acad. Sci. U S A. *102*, 15545–15550.

Sugimoto, M., Wong, D.T., Hirayama, A., Soga, T., and Tomita, M. (2010). Capillary electrophoresis mass spectrometry-based saliva metabolomics identified oral, breast and pancreatic cancer-specific profiles. Metabolomics *6*, 78–95.

Sugiyama, E., Togashi, Y., Takeuchi, Y., Shinya, S., Tada, Y., Kataoka, K., Tane, K., Sato, E., Ishii, G., Goto, K., et al. (2020). Blockade of EGFR improves responsiveness to PD-1 blockade in EGFR-mutated non-small cell lung cancer. Sci. Immunol. *5*. https://doi.org/10.1126/sciimmunol.aav3937.

Tada, Y., Togashi, Y., Kotani, D., Kuwata, T., Sato, E., Kawazoe, A., Doi, T., Wada, H., Nishikawa, H., and Shitara, K. (2018). Targeting VEGFR2 with Ramucirumab strongly impacts effector/activated regulatory T cells and CD8+ T cells in the tumor microenvironment. J. Immunother. Cancer *6*, 106.

Takeuchi, Y., Tanemura, A., Tada, Y., Katayama, I., Kumanogoh, A., and Nishikawa, H. (2018). Clinical response to PD-1 blockade correlates with a sub-fraction of peripheral central memory CD4+ T cells in patients with malignant melanoma. Int. Immunol. *30*, 13–22.

Tanegashima, T., Togashi, Y., Azuma, K., Kawahara, A., Ideguchi, K., Sugiyama, D., Kinoshita, F., Akiba, J., Kashiwagi, E., Takeuchi, A., et al. (2019). Immune suppression by PD-L2 against spontaneous and treatment-related antitumor immunity. Clin. Cancer Res. *25*, 4808–4819.

Thommen, D.S., Koelzer, V.H., Herzig, P., Roller, A., Trefny, M., Dimeloe, S., Kiialainen, A., Hanhart, J., Schill, C., Hess, C., et al. (2018). A transcriptionally and functionally distinct PD-1+ CD8+ T cell pool with predictive potential in non-small-cell lung cancer treated with PD-1 blockade. Nat. Med. *24*, 994–1004.

Togashi, Y., Shitara, K., and Nishikawa, H. (2019). Regulatory T cells in cancer immunosuppression—implications for anticancer therapy. Nat. Rev. Clin. Oncol. *16*, 356–371.

Topalian, S.L., Hodi, F.S., Brahmer, J.R., Gettinger, S.N., Smith, D.C., McDermott, D.F., Powderly, J.D., Sosman, J.A., Atkins, M.B., Leming, P.D., et al. (2019). Five-year survival and correlates among patients with advanced melanoma, renal cell carcinoma, or non-small cell lung cancer treated with nivolumab. JAMA Oncol. *5*, 1411–1420.

Topper, M.J., Vaz, M., Chiappinelli, K.B., DeStefano Shields, C.E., Niknafs, N., Yen, R.C., Wenzel, A., Hicks, J., Ballew, M., Stone, M., et al. (2017). Epigenetic therapy ties MYC depletion to reversing immune evasion and treating lung cancer. Cell *171*, 1284–1300.e1.

Tran, D.Q., Ramsey, H., and Shevach, E.M. (2007). Induction of FOXP3 expression in naive human CD4+FOXP3 T cells by T-cell receptor stimulation is transforming growth factor-beta dependent but does not confer a regulatory phenotype. Blood *110*, 2983–2990.

Trapnell, C., Roberts, A., Goff, L., Pertea, G., Kim, D., Kelley, D.R., Pimentel, H., Salzberg, S.L., Rinn, J.L., and Pachter, L. (2012). Differential gene and transcript expression analysis of RNA-seq experiments with TopHat and Cufflinks. Nat. Protoc. *7*, 562–578.

Wang, H., Franco, F., and Ho, P.C. (2017). Metabolic regulation of Tregs in cancer: opportunities for immunotherapy. Trends Cancer *3*, 583–592.

Wang, R., Dillon, C.P., Shi, L.Z., Milasta, S., Carter, R., Finkelstein, D., McCormick, L.L., Fitzgerald, P., Chi, H., Munger, J., et al. (2011). The transcription factor Myc controls metabolic reprogramming upon T lymphocyte activation. Immunity *35*, 871–882.

Warburg, O. (1956). On the origin of cancer cells. Science *123*, 309–314.

Watson, M.J., Vignali, P.D.A., Mullett, S.J., Overacre-Delgoffe, A.E., Peralta, R.M., Grebinoski, S., Menk, A.V., Rittenhouse, N.L., DePeaux, K., Whetstone, R.D., et al. (2021). Metabolic support of tumour-infiltrating regulatory T cells by lactic acid. Nature *591*, 645–651.

Weinberg, S.E., Singer, B.D., Steinert, E.M., Martinez, C.A., Mehta, M.M., Martinez-Reyes, I., Gao, P., Helmin, K.A., Abdala-Valencia, H., Sena, L.A., et al. (2019). Mitochondrial complex III is essential for suppressive function of regulatory T cells. Nature *565*, 495–499.

Wherry, E.J., and Kurachi, M. (2015). Molecular and cellular insights into T cell exhaustion. Nat. Rev. Immunol. *15*, 486–499.

Wiig, H., Aukland, K., and Tenstad, O. (2003). Isolation of interstitial fluid from rat mammary tumors by a centrifugation method. Am. J. Physiol. Heart Circ. Physiol. *284*, H416–H424.

Williams, M.A., and Bevan, M.J. (2007). Effector and memory CTL differentiation. Annu. Rev. Immunol. *25*, 171–192.

Wing, K., Onishi, Y., Prieto-Martin, P., Yamaguchi, T., Miyara, M., Fehervari, Z., Nomura, T., and Sakaguchi, S. (2008). CTLA-4 control over Foxp3+ regulatory T cell function. Science *322*, 271–275.

Wu, Y., Borde, M., Heissmeyer, V., Feuerer, M., Lapan, A.D., Stroud, J.C., Bates, D.L., Guo, L., Han, A., Ziegler, S.F., et al. (2006). FOXP3 controls regulatory T cell function through cooperation with NFAT. Cell *126*, 375–387.

Xu, Y., Poggio, M., Jin, H.Y., Shi, Z., Forester, C.M., Wang, Y., Stumpf, C.R., Xue, L., Devericks, E., So, L., et al. (2019). Translation control of the immune checkpoint in cancer and its therapeutic targeting. Nat. Med. *25*, 301–311.

Yamamoto, H., Fujimori, T., Sato, H., Ishikawa, G., Kami, K., and Ohashi, Y. (2014). Statistical hypothesis testing of factor loading in principal component analysis and its application to metabolite set enrichment analysis. BMC Bioinformatics *15*, 51.

Yu, J., Green, M.D., Li, S., Sun, Y., Journey, S.N., Choi, J.E., Rizvi, S.M., Qin, A., Waninger, J.J., Lang, X., et al. (2021). Liver metastasis restrains immunotherapy efficacy via macrophage-mediated T cell elimination. Nat. Med. *27*, 152–164.

Zappasodi, R., Serganova, I., Cohen, I.J., Maeda, M., Shindo, M., Senbabaoglu, Y., Watson, M.J., Leftin, A., Maniyar, R., Verma, S., et al. (2021). CTLA-4 blockade drives loss of T(reg) stability in glycolysis-low tumours. Nature *591*, 652–658.

Zou, W., Wolchok, J.D., and Chen, L. (2016). PD-L1 (B7-H1) and PD-1 pathway blockade for cancer therapy: mechanisms, response biomarkers, and combinations. Sci. Transl. Med. *8*, 328rv324.

STAR★METHODS

KEY RESOURCES TABLE

REAGENT or RESOURCE	SOURCE	IDENTIFIER
Antibodies		
Anti-human CD3-Alexa Fluor 700 (UCHT1)	BD Biosciences	Cat# 557943; RRID: AB_396952
Anti-human CD4-V500 (RPA-T4)	BD Biosciences	Cat# 560768; RRID: AB_1937323
Anti-human CD8a-Brilliant Violet 785 (RPA-T8)	Biolegend	Cat# 301046; RRID: AB_11219195
Anti-human CD45RA-Brilliant Violet 711 (HI100)	Biolegend	Cat# 304138; RRID: AB_2563815
Anti-human FOXP3-PE (236A/E7)	eBioscience	Cat# 12-4777-42; RRID: AB_1944444
Anti-human CD152-APC (L3D10)	Biolegend	Cat# 349908; RRID: AB_10679122
Anti-humam PD-1-Brilliant Violet421 (MIH4)	BD Biosciences	Cat# 564323; RRID: AB_2738745
Anti-human CD147-PerCP/Cyanine5.5 (HIM6)	BD Biosciences	Cat# 562554; RRID: AB_2737650
Anti-MCT1-Alexa Fluor 647	novus	Cat# NBP1-59656AF647
Anti-LDHB-FITC	novus	Cat# NBP2-53421F
Anti-mouse CD3-Alexa Fluor 700 (17A2)	eBioscience	Cat# 56-0032-82; RRID: AB_529507
Anti-mouse CD4-V500 (RM4-5)	BD Biosciences	Cat# 560782; RRID: AB_1937315
Anti-mouse CD8a-Brilliant Violet 785 (53-6.7)	Biolegend	Cat# 100750; RRID: AB_2562610
Anti-mouse FOXP3-PE (FJK-16s)	eBioscience	Cat# 12-5773-82; RRID: AB_465936
Anti-mouse CD279 (PD-1)-APC (29F.1A12)	Biolegend	Cat# 135209; RRID: AB_2251944
Anti-mouse CD279 (PD-1)-Brilliant Violet 421 (29F.1A12)	Biolegend	Cat# 135217; RRID: AB_10900085
Anti-mouse CD152 (CTLA-4)-APC (UC10-4B9)	eBioscience	Cat# 17-1522-82; RRID: AB_2016700
Anti-mouse CD134 (OX40) Brilliant Violet711(OX-40)	BD Biosciences	Cat# 745449; RRID: AB_2742993
Anti-mouse CD278 (ICOS) FITC (7E.17G9)	eBioscience	Cat# 11-9942-82; RRID: AB_11218290
Anti-mouse CD357 (GITR) PE/Cy7 (YGITR 765)	Biolegend	Cat# 120222; RRID: AB_528907
Anti-mouse CD45.2-V500 (104)	BD Biosciences	Cat# 562129; RRID: AB_10897142
Anti-mouse I-A^d-FITC (39-10-8)	Biolegend	Cat# 115005; RRID: AB_313620
Anti-mouse CD11b-BUV395 (M1/70)	BD Biosciences	Cat# 563553; RRID: AB_2738276
Anti-mouse CD11c-Brilliant Violet 605 (HL3)	BD Biosciences	Cat# 563057; RRID: AB_2737978
Anti-mouse CD80-Brilliant Violet 421 (16-10A1)	Biolegend	Cat# 104725; RRID: AB_10900989
Anti-mouse CD86-PE/Cy7 (GL-1)	Biolegend	Cat# 105013; RRID: AB_439782
Anti-mouse Ki-67-PerCP/Cyanine5.5 (16A8)	Biolegend	Cat# 652423; RRID: AB_2629530
Anti-mouse CD147-Brilliant Violet 480 (RL73)	BD Biosciences	Cat# 746282; RRID: AB_2743612
Anti-mouse TNF-α-Brilliant Violet 421 (MP6-XT22)	Biolegend	Cat# 506327; RRID: AB_10900823
Anti-mouse IFN gamma-FITC (XMG1.2)	eBioscience	Cat# 11-7311-82; RRID: AB_465412
Anti-mouse CD62L-BV711 (MEL-14)	BD Biosciences	Cat# 740660; RRID: AB_2740349
Anti-mouse CD44-BUV395 (IM7)	BD Biosciences	Cat# 740215; RRID: AB_2739963
Mouse IgG1 isotype control-APC (MOPC-21)	BD Biosciences	Cat# 550854; RRID: AB_398467

(Continued on next page)

Continued

REAGENT or RESOURCE	SOURCE	IDENTIFIER
Mouse IgG1 isotype control-Brilliant Violet 785 (MOPC-21)	Biolegend	Cat# 400170; RRID: AB_2460666
Mouse IgG1 isotype control-Brilliant Violet 711 (X40)	BD Biosciences	Cat# 563044; RRID: AB_2869449
Rat IgG2b isotype control-FITC (RTK4530)	Biolegend	Cat# 400605; RRID: AB_326549
Rat IgG2b isotype control-PE/Cy7 (RTK4530)	Biolegend	Cat# 400618; RRID: AB_326560
Amenian Hamster IgG isotype control-PE/Cy7 (HTK888)	Biolegend	Cat# 400921
Mouse IgG2b isotype control-Alexa Fluor 488 (27-35)	BD Biosciences	Cat# 558716; RRID: AB_1645613
Rabbit IgG isotype control-Alexa Fluor 647 (EPR25A)	abcam	Cat# ab199093; RRID: AB_2818935
Rabbit IgG isotype control-PE	novus	Cat# NBP2-24983
Armenian Hamster IgG isotype control-Brilliant Violet 421 (HTK888)	Biolegend	Cat# 400935; RRID: AB_10896426
Rat IgG2a κ isotype control-PE/Cy7 (RTK2758)	Biolegend	Cat# 400522; RRID: AB_326542
Hamster IgG2, λ1 isotype control-BV605 (Ha4/8)	BD Biosciences	Cat# 563056; RRID: AB_2869454
Mouse IgG1 isotype control-FITC (MOPC-21)	Biolegend	Cat# 400107; RRID: AB_326429
Anti-β-actin	Cell Signaling Technology	Cat# 4967S; RRID: AB_330288
Anti-human CD3 (SP7)	abcam	Cat# ab16669; RRID: AB_443425
Anti-human CD4 (4B12)	DAKO	Cat# M731029-2
Anti-human CD8 (C8/144B)	DAKO	Cat# M710301-2
Anti-human FOXP3 (236A/E7)	abcam	Cat# ab20034; RRID: AB_445284)
Anti-human PD-1 (clone EPR4877(2))	abcam	Cat# ab137132; RRID: AB_2894867
Anti-human LDHA (C4B5)	Cell Signaling Technology	Cat# 3582; RRID: AB_2066887
Anti-human PDHK1 (PDK1) (C47H1)	Cell Signaling Technology	Cat# 3820; RRID: AB_1904078
Anti-human HIF1α (mgc3)	abcam	Cat# ab16066; RRID: AB_302234
Anti-human MYC (Y69)	abcam	Cat# ab32072; RRID: AB_731658
Anti-histon H3 (D1H2)	Cell Signaling Technology	Cat# 4499; RRID: AB_10544537
Anti-NFAT1 (D43B1)	Cell Signaling Technology	Cat# 5861; RRID: AB_10834808
Anti-c-Myc (9E10)	novus	Cat# NB600-302SS
Anti-Hexokinase II (3D3)	abcam	Cat# ab104836; RRID: AB_10710018
Anti-HK2 (H.738.7)	Thermo Fisher Scientific	Cat# MA5-14849; RRID: AB_10987229
Anti-PDK1 (4A11)	abcam	Cat# ab110025; RRID: AB_10865315
Anti-LDHA	Cell Signaling Technology	Cat#2012; RRID: AB_2137173
Anti-Lactate Dehydrogenase B [60H11]	abcam	Cat# ab85319; RRID: AB_1860766
Anti-MCT1	abcam	Cat# ab93048; RRID: AB_10563650
Goat Anti-Rabbit IgG H&L (HRP)	abcam	Cat# ab6721; RRID: AB_955447
Goat Anti-Mouse IgG H&L (HRP)	abcam	Cat# ab6789; RRID: AB_955439
Nivolumab	ONO pharmaceutical	kindly gifted
Purified anti-human CD3 (OKT3)	eBioscience	Cat# 16-0037-81; RRID: AB_468854
Purified anti-human CD28 (CD28.2)	eBioscience	Cat# 14-0289-82; RRID: AB_467194
Purified anti-mouse CD3 (17A2)	eBioscience	Cat# 14-0032-82; RRID: AB_467053
Purified anti-mouse CD28 (37.51)	eBioscience	Cat# 14-0281-82; RRID: AB_467190
Purified anti-mouse PD-1 (RMP1-14)	Biolegend	Cat# 114116; RRID: AB_2566280
Purified Rat IgG, κ isotype control(RTK2758)	Biolegend	Cat# 400533; RRID: AB_2861021

Continued

REAGENT or RESOURCE	SOURCE	IDENTIFIER
Purified Anti-Mouse CD16/CD32	BD Biosciences	Cat# 553141; RRID: AB_394656
Fc Receptor Binding Inhibitor Functional Grade Polyclonal Antibody	eBioscience	Cat# 16-9161-73; RRID: AB_469272
Biological samples		
healthy donor PBMC	CTL	N/A
Chemicals, peptides, and recombinant proteins		
Fetal Bovine Serum	Biosera	Cat# FB-1061/500
ECL Prime Western Blotting Detection Reagent	GE Healthcare	Cat# RPN2236
RPMI 1640 Medium	Fujifilm Wako	Ca# 189-02,025
RPMI 1640 Medium, no Glucose	ThermoFisher	Cat# 11879020
D-(+)-Glucose	Sigma-Aldrich	Cat# G8270-100G
GSK2837808A	Adipogen Corporation	Cat# AG-CR1-3685
AR-C155858	ChemScene LLC	Cat# CS-0540
Phorbol 12-myristate 13-acetate (PMA)	Sigma-Aldrich	Cat# P8139
Ionomycin	Sigma-Aldrich	Cat# I0634
Hygromycin	Fujifilm Wako	Cat# 084-07681
Puromycin	ThermoFisher	Cat# A1113802
Critical commercial assays		
Fixable Viability Dye eFluor™ 780	eBioscience	Cat# 65-0865-14
H-2Kb MuLV p15E tetramer-KSPWFTTL-APC	MBL	Cat# TS-M507-2
T-Select H-2Kb β-galactosidase Tetramer-DAPIYTNV-APC	MBL	Cat# TS-M501-2
Annexin V-FITC	Biolegend	Cat# 640906
7-AAD	ThermoFisher	Cat# A1310
NEBNext Ultra Directional RNA Library Prep Kit	New England BioLabs	Cat# E7420
QIAamp DNA Mini Kit	QIAGEN	Cat# 51304
RNeasy Mini Kit	QIAGEN	Cat# 74104
TRIzol Reagent	Thermo Fisher Scientific	Cat# 15596026
Nextera XT DNA Sample Preparation Kit	Illumina	Cat# FC-131-1024
SMART-Seq v4 Ultra Low Input RNA Kit	Takara Bio	Cat# 634888
Oncomine™ Comprehensive Assay version 3	Thermo Fisher Scientific	Cat# A35805
Oncomine ™ Cancer Research Panel	Thermo Fisher Scientific	N/A
Opal Polaris 7 Color Manual IHC Detection Kit	PerkinElmer	Cat# NEL861001KT
Lactate Colorimetric/Fluorometric Assay Kit	BioVision	Cat# K607-100
Foxp3/Transcription Factor Staining Buffer Set	eBioscience	Cat# 00-5523-00
7-AAD Viability Staining Solution	eBioscience	Cat# 00-6993-50
Fluo-8/AM	AAT Bioquest	Cat# 21080
Carboxyfluorescein succinimidyl ester	Thermo Fisher Scientific	Cat# C34554
Agilent G1603A CE-MS adapter kit	Agilent Technologies	N/A
Agilent G1607A CE-ESI-MS sprayer kit	Agilent Technologies	N/A
Recombinant IL-2	R & D systems	Cat# 202-IL-010
Recombinant IL-7	PEPROTECH	Cat# AF-200-07
Lactic acid	Sigma-Aldrich	N/A

(Continued on next page)

Continued

REAGENT or RESOURCE	SOURCE	IDENTIFIER
Deposited data		
RNA sequencing data of surgically resected GCs	Kumagai et al. (2020b)	GEO: GSE152040
RNA sequencing data of surgically resected NSCLCs	This paper	GEO: GSE190139
RNA sequencing data of TILs extracted from surgically resected NSCLCs	This paper	GEO: GSE190141
Chip sequencing data of Treg cells from healthy human PBMCs	Birzele et al. (2011)	SRP006674
Chip sequencing data of Treg cells from healthy human PBMCs	Schmidl et al. (2014)	GEO: GSE43119
Experimental models: Cell lines		
Jurkat E6.1	KAC	Cat# EC88042803-F0
B16-F10	ATCC	Cat# CRL-6475
MC-38	Kerafast	Cat# ENH204
Experimental models: Organisms/strains		
C57BL/6	CLEA	N/A
C57BL/6, $Foxp3^{thy1.1}$		kindly gifted by Dr. Alexander Rudensky
C57BL/6, Scid	Riken BioResource Research Center	kindly provided by Dr. Kagemasa Kuribayashi
C57BL/6, $Slc16a1$ knocked-out	Cyagen	in this study
C57BL/6, $Slc16a1$ floxed	Cyagen	in this study
C57BL/6, $Foxp3^{Cre}YFP$	Jackson Laboratory	kindly gifted by Dr. Alexander Rudensky
Recombinant DNA		
pBABE puro	Addgene	Cat# 1764
pMX-IRES-GFP vector	Addgene	N/A
pMMLV-hygro-CMV vector	VectorBuilder	N/A
SMARTvector lentiviral shRNA	Horizon Discovery	N/A
Mouse $Slc16a1$ forward primer: GGC AGC CGT CCA GTA ATG AT	FASMAC	in this study
Mouse $Slc16a1$ reverse primer: TGA AAG CAA GCC CAA GAC CT	FASMAC	in this study
Mouse $18sr$ forward primer: TAG AGT GTT CAA AGC AGG CCC	FASMAC	in this study
Mouse $18sr$ reverse primer: CCA ACA AAA TAG AAC CGC GGT	FASMAC	in this study
Software and algorithms		
FlowJo 10.0.8	BD Biosciences	N/A
GraphPad Prism 9.1.0	GraphPad Software Inc.	N/A
iForm 2.5.0	PerkinElmer	N/A
GSEA 4.1.0	Broad Institute	N/A
ImageJ	Schneider et al. (2012)	https://imagej.nih.gov/ij/
R version 3.1.1	R Foundation for Statistical Computing	N/A

RESOURCE AVAILABILITY

Lead contact
Please direct any requests for further information or reagents to the lead contact, Hiroyoshi Nishikawa (hnishika@ncc.go.jp).

Material availability

Mouse lines generated in this study can be available from the lead contact upon request. Further information and requests for resources and reagents should be directed to and will be fulfilled by the lead contact.

Data and code availability

The accession numbers for the RNA-seq data of surgically resected NSCLCs and TILs extracted from NSCLCs reported in this paper are GEO: GSE190139, and GEO: GSE190141, respectively. As for surgically resected GC samples, we have already deposited RNA-seq data (GEO: GSE152040) and reanalyzed the data in this study (Kumagai et al., 2020b). Raw FASTQ files for FOXP3 ChIP-seq data were downloaded from the Gene Expression Omnibus with the accession codes GSE43119 (Schmidl et al., 2014) and SRP006674 (Birzele et al., 2011).

EXPERIMENTAL MODEL AND SUBJECT DETAILS

Patients and samples

Patients with GC or NSCLC who underwent surgical resection at National Cancer Center Hospital East were enrolled in this study (summarized in Tables S1 and S2). Patients harboring advanced NSCLC with liver metastatic lesions who received liver biopsy at National Cancer Center Central Hospital were also enrolled in this study (summarized in Table S3). In addition, patients with advanced GC, NSCLC or MM who received PD-1 blockade monotherapy (nivolumab or pembrolizumab) at National Cancer Center Central Hospital or Hospital East were enrolled in this study (summarized in Tables S4–S8). PBMCs were isolated by density gradient centrifugation with Ficoll-Paque (GE Healthcare, Chicago, IL). To collect TILs, tumor tissues were minced and treated within 72h after surgery with a TIL preparation protocol using an optimized tissue preservation reagent (Tumor & Tissue Preservation Reagent: TTPR) and TIL isolation reagent (Tumor & Tissue Dissociation Reagent: TTDR) co-developed with BD Biosciences (Franklin Lakes, NJ)(details in PCT/JP2020/005991) or treated immediately with a gentleMACS Dissociator (Miltenyi Biotec, Bergisch Gladbach, Germany) as described previously (Kumagai et al., 2020a, 2020b; Saito et al., 2016; Tada et al., 2018). All patients provided written informed consent before sampling, according to the Declaration of Helsinki. This study was performed in a blinded manner and was approved by the National Cancer Center Ethics Committee.

Cell lines and reagents

MC-38 and B16-F10 mouse colon cancer cell lines were obtained from Kerafast (Boston, MA; Cat#ENH204, RRID: B288) and ATCC (Cat#CRL-6475, RRID: CVCL_0159), respectively. Jurkat E6.1, a human T cell leukemia cell line, was obtained from KAC Co., Ltd (Kyoto, Japan) (Cat# EC88042803-F0, RRID: CVCL_0367). B16-OVA is a cell line derived from B16-F10 cells stably transfected with OVA, using a pBabe-puro vector (Addgene, Cat#1764, Cambridge, MA). All cell lines were maintained in Roswell Park Memorial Institute (RPMI) medium (Fujifilm Wako Pure Chemical Corporation, Osaka, Japan) supplemented with 10% fetal bovine serum (FBS; Biosera, Orange, CA). The murine *Myc* (T58A mutation)-overexpressing cell lines were established via retroviral transduction using pMMLV-hygro-CMV vector (VectorBuilder, Chicago IL). The human *FOXP3*-overexpressing cell lines were established by retroviral transduction using pMX-IRES-GFP vector (Addgene). The murine Ldha knocked-down cell lines were established by lentiviral transduction using SMARTvector lentiviral shRNA (Horizon Discovery, Cambridge, UK) and were stemmed from a single clone. GSK2837808A and AR-C155858 were obtained from Adipogen Corporation (San Diego, CA) and ChemScene LLC (Monmouth Junction, NJ), respectively. Anti-PD-1 mAb (RMP1-14) and control rat IgG mAb (RTK2758) used in the *in vivo* study were obtained from BioLegend (San Diego, CA).

In vivo animal models

Female C57BL/6 mice (6- to 10-week-old females; CLEA Japan, Tokyo, Japan), C57/BL6scid mice (Riken BioResource Research Center, Tsukuba, Japan: kindly provided by Dr. Kagemasa Kuribayashi in Mie University, Mie, Japan), *Foxp3*thy1.1 mice, *Foxp3*Cre mice (Memorial Sloan Kettering Cancer Center, NY: kindly gifted by Dr. Alexander Rudensky), *Slc16a1* knocked-out mice, and *Slc16a1* floxed mice were used for the *in vivo* studies. The mice were housed in cages under specific pathogen-free conditions, provided with standard food, given free access to hypochlorous weak-acid water, and on a 12:12 light/dark cycle with lights on at 8:00 am. The temperature was kept at 22 °C (20–26 °C) and humidity at 45% (40–60%). Animal care and experiments were conducted according to the guidelines of the animal committee of the National Cancer Center after approval by the Ethics Review Committee for Animal Experimentation of the National Cancer Center. A suspension of 1×10^6 cells (in 100 μL of PBS) was injected subcutaneously or directly into the lung or the liver of mice. In some groups, anti-PD-1 mAb (200 μg/body) was administered intravenously three times at three-day intervals with or without GSK2837808A (6 mg/kg) administered orally for ten days. In other experiments, AR-C155858 (10 mg/kg) was administered intraperitoneally daily for ten days combined with or without anti-PD-1 mAb. Tumor volume was calculated as the length × width^2 × 0.5. Mice were monitored twice a week and sacrificed when tumor volume was >1800 mm^3. For TIL analyses, tumors were collected twelve days after tumor cell injection. Cell$^+$ counts were calculated with FCM, and cell counts per weight were evaluated. To examine tumor (MC38) antigen-specific CD8$^+$ T cells, T-Select H-2Kb MuLV p15E Tetramer-KSPWFTTL-APC (MBL, Nagoya, Japan) was used according to the manufacturer's instructions. For intracellular cytokine assays, cells were stimulated for 5 h with phorbol 12-myristate 13-acetate (PMA; 100 ng/mL)/ionomycin (2 μg/mL) (Sigma-Aldrich, St. Louis,

MO). GolgiPlug reagent (1.3 μL/mL) (BD Biosciences) was added for the last 4 hours of the culture, and then stained cells were subjected to FCM. All *in vivo* experiments were performed at least twice.

METHOD DETAILS

Generation of Slc16a1 knocked-out and conditional knocked-out mice

Slc16a knocked-out (KO) mice (C57BL/6J) were generated by CRISPR/Cas-mediated genome engineering (Cyagen Biosciences (Suzhou) Inc.). The mouse Slc16a1 gene (GenBank accession number: NM_009196.4; Ensembl: ENSMUSG00000032902) is located on mouse chromosome 3. Exon 2 to exon 5 were selected as the target site. Two pairs of gRNA targeting vectors were constructed and confirmed by sequencing. gRNA target sequences were as follows: gRNA1 (matches forward strand of the gene); TATCAGT CCATTGGAGTTGTAGG and gRNA2 (matches forward strand of the gene); CGCGCGAAGCTGCATTTGCTGGG. Cas9 mRNA and gRNA generated by *in vitro* transcription were co-injected into fertilized eggs for KO mouse production. F0 founder animals were genotyped by PCR followed by sequence analysis and crossed with each other. F1 founder animals were identified by PCR followed by sequence analysis and bred to heterozygous mice to test germline transmission and F2 animal generation. Genotypes for *Slc16a1* KO mice were performed by PCR with the following primer pairs: *Slc16a1* KO forward, AAACTCCTGCTTTGCTGATTTCCTAGT; *Slc16a1* KO reverse, CTGATAGCCACGATAGAGAATGAGGAAG (annealing temperature: 60°C, detected band size for *Slc16a1* KO: 574bp); wild-type forward, AAGTGGATCAGACCTCGGATC; wild-type reverse, GTTTAGTAACCCAAGCTCTCAAAT (annealing temperature: 60°C, detected band size for wild-type: 568bp). To create a mouse Slc16a1 conditional knocked-out (cKO) model in C57BL/6J mice by CRISPR/Cas-mediated genome engineering: exon 3 and exon 4 that cover 66.94% of the coding region were selected as the conditional knockout region. Cas9 mRNA and gRNA were co-injected into fertilized eggs with a targeting vector for mice production. F0 founder animals were genotyped by PCR followed by sequencing analysis and bred to wildtype mice to test germline transmission and F1 animal generation. gRNA target sequences were as follows: gRNA1 (matches reverse strand of the gene); TGCCAGGTTACAGCGGACACTGG and gRNA2 (matches forward strand of the gene): CATTATATAATTTGAGAGCTTGG. Heterozygous F1 mice were crossed with each other to generate homozygous F2 mice. Genotypes for *Slc16a1* cKO mice were performed by PCR with the following primer pairs: forward, GCCTCTTGCTACTTAGTACTCTTG; reverse, TTGAGGAACAAATG ACTGCTTACAG with annealing temperature: 60°C [detected band sizes are one band with 210 bp (homozygous), two bands with 210 bp and 146 bp (heterozygous), one band with 146 bp (wild-type)]. *Slc16a1* cKO mice were crossed with *Foxp3*[Cre] mice (The Jackson Laboratory, Bar Harbor, ME: kindly gifted by Dr. Alexander Rudensky, Memorial Sloan Kettering Cancer Center, New York, NY). For all comparisons, littermate controls were used.

RNA-seq for tumor samples

Total RNA was extracted from tumor samples with an RNeasy Mini Kit (Qiagen, Hilden, Germany) according to the manufacturer's instructions. RNA integrity was evaluated with TapeStation (Agilent Technologies, Santa Clara, CA). Complementary DNA (cDNA) was prepared from the isolated RNA using a NEBNext Ultra Directional RNA Library Prep Kit (New England BioLabs, Ipswich, MA) in which cDNA is prepared from polyA-selected RNA. The prepared RNA-seq libraries underwent next-generation sequencing of 120 bp from both ends (paired-end reads) with a HiSeq2500 platform (Illumina, San Diego, CA). For expression profiling with the RNA-seq data, paired-end reads were aligned to the hg38 human genome assembly using TopHat2 (https://ccb.jhu.edu/software/tophat/index.shtml) (Kim et al., 2013). The expression level of each RefSeq gene was calculated from the mapped read counts using Cufflinks (http://cufflinks.cbcb.umd.edu) (Trapnell et al., 2012). GSEA version 4.1.0 (Massachusetts Institute of Technology, Cambridge, MA) were used for statistical analyses.

RNA-seq for TILs

PD-1^{+}, PD-1^{-} CD8^{+} T cells and CD45RA^{-}CD25^{high}CD4^{+} T cells (eTreg cells) were sorted from four surgically resected NSCLC samples. Total RNA was extracted using TRIzol (Invitrogen) according to the manufacturer's instructions. cDNA was prepared from the isolated RNA using a SMART-Seq v4 Ultra Low Input RNA Kit (Takara Bio). The RNA-seq libraries were prepared using the amplified cDNA and a Nextera XT DNA Sample Preparation Kit (Illumina). The prepared RNA-seq libraries underwent next-generation sequencing of 100 bp from both ends (paired-end reads) with a Novaseq 6000 platform (Illumina).

Real-time reverse transcription PCR (qRT-PCR)

RNA was extracted using the RNeasy Mini Kit (QIAGEN), cDNA was generated using SuperScript VILO IV (Thermo Fisher Scientific), and real-time qRT-PCR was performed with or SYBR Green reagents (Thermo Fisher Scientific) using the QuantStudio 7 Flex Real-Time PCR System (Thermo Fisher Scientific). Gene expression change of murine *Slc16a1* (forward primer: GGC AGC CGT CCA GTA ATG AT, reverse primer: TGA AAG CAA GCC CAA GAC CT) relative to the expression of *18S* ribosomal RNA (forward primer: TAG AGT GTT CAA AGC AGG CCC, reverse primer: CCA ACA AAA TAG AAC CGC GGT), which was used as a housekeeping gene, were calculated using the DDCT method. The primers used in this study are listed in key resources table.

WES and mutational analysis

DNA was extracted with the QIAmp DNA Mini Kit (QIAGEN) according to the manufacturer's instructions. Sequencing libraries were prepared for WES with a NEBNext Ultra DNA Library Prep Kit (New England BioLabs) according to the manufacturer's instructions.

Adaptor-ligated samples were amplified with six PCR cycles. The amplified DNA fragments underwent enrichment for the exonic fragments using a SureSelect Human All Exon Kit v5 (Agilent Technologies). Massively parallel sequencing of the isolated fragments was performed with a HiSeq2500 platform (Illumina). Paired-end WES reads were independently aligned to the human reference genome (hg38) using BWA (Li and Durbin, 2009), Bowtie2 (http://bowtie-bio.sourceforge.net/bowtie2/index.shtml), and NovoAlign (http://www.novocraft.com/products/novoalign/). Somatic mutations were called using MuTect (http://www.broadinstitute.org/cancer/cga/mutect), SomaticIndelDetector (http://www.broadinstitute.org/cancer/cga/node/87), and VarScan (http://varscan.sourceforge.net). Mutations were discarded if (I) the read depth was < 20 or the variant allele frequency (VAF) was < 0.1, (II) they were supported by only one strand of the genome, or (III) they were present in the normal human genomes in either the 1000 Genomes Project dataset (http://www.internationalgenome.org/) or our in-house database. Gene mutations were annotated by SnpEff (http://snpeff.sourceforge.net). To detect *MYC* amplifications, genomic alterations were assessed using Oncomine™ Comprehensive Assay version 3 or Oncomine ™ Cancer Research Panel (Thermo Fisher Scientific, Waltham, MA).

Gene expression data analysis

Enriched pathways were determined using the GSEA tool available from the Broad Institute website. Hallmark gene sets were downloaded from the MSigDB database (Subramanian et al., 2005). Significantly enriched gene expression between two groups was detected by differential gene expression analysis using the package of edgeR (Robinson et al., 2010), and the results were demonstrated in volcano plots by using R version 4.1.0 (R Foundation for Statistical Computing, Vienna, Austria).

ChIP-seq data processing

Trim-Galore was used for trimming adaptor sequence and filtering low quality reads. We then aligned filtered FASTQ files to mm10 genome using Bowtie 2. The duplicated reads and reads having mapping quality < 4 were filtered out using Picard Tools and samtools (Li et al., 2009), respectively. ChIP-seq peaks were identified for each sample using MACS2.

FCM analysis

FCM staining and analysis were performed as described (Kumagai et al., 2020a, Kumagai et al., 2020b; Tada et al., 2018; Takeuchi et al., 2018; Tanegashima et al., 2019). The antibodies used in the FCM analyses are summarized in key resources table. Briefly, cells were washed with a washing solution and subjected to staining with surface antibodies and a fixable viability dye (Thermo Fisher Scientific). Then, intracellular staining was performed with intracellular antibodies and a Foxp3/Transcription Factor Staining Buffer Set (Thermo Fisher Scientific) according to the manufacturer's instructions. After washing, the cells were analyzed with an LSR Fortessa or Symphony instrument (BD Biosciences) and FlowJo software (BD Biosciences).

Evaluation of Ca^{2+} concentration

Free Ca^{2+} concentration was detected by FCM with a Fluo-8/AM (AAT Bioquest). Cells were loaded with the Fluo-8/AM at 37°C in the dark at a final concentration of 5 μM in a complete culture medium. After 30 min incubation, the cells were washed twice to remove excess probes and resuspended in PBS (500 μL). After washing, the cells were analyzed with an LSR Fortessa or Symphony instrument (BD Biosciences) and FlowJo software (BD Biosciences).

Apoptosis analysis

Apoptosis was assessed by FCM with FITC-annexin V, 7-AAD (Thermo Fisher Scientific), and active caspase-3 staining. The dilution of the staining reagents was performed according to the manufacturer's instructions.

Proliferation analysis

Proliferation was evaluated by dilution of carboxyfluorescein succinimidyl ester (CFSE, Thermo Fisher Scientific)-labelled cells with FCM. The dilution of the staining reagents was performed according to the manufacturer's instructions.

IHC

Tumor samples collected from surgically resection, endoscopic biopsy or fine needle biopsy were fixed in formalin, paraffin-embedded, and sectioned onto slides for IHC. The slides were deparaffinized with xylene, rehydrated, and antigen-retrieved in a microwave oven for 20 min. After the inhibition of endogenous peroxidase activity, individual slides were then incubated overnight at 4°C with anti-human LDHA (clone: C4B5, Cell Signaling Technology, Danvers MA), anti-human PDHK1 (PDK1) (clone: C47H1, Cell Signaling Technology), anti-human HIF1α (clone: mgc3, Abcam) and anti-human MYC (clone: Y69, Abcam) mAbs. The slides were then incubated with EnVision reagent (Dako, Glostrup, Denmark), and a color reaction was developed using 2% 3,3-diaminobenzidine in 50 mM tris buffer (pH 7.6) containing 0.3% hydrogen peroxidase; these sections were finally counterstained with Meyer hematoxylin. The staining intensity was graded as 0 (no staining); 1+ (weak); 2+ (moderate); or 3+ (strong). The IHC scores were evaluated as follows: staining score (0–3) = sum of each staining intensity (0–3) multiplied by the percentage of tumor cells (0–100%). The high expression of each molecule was defined as more than or equal to the IHC score of 2. For MYC staining, positively stained cells were counted in five files and percentages of positive cells in total cancer cells were calculated. High expression of MYC was defined as tumors with more than or equal to 50% of positive cells of total cancer cells. Multiplexed fluorescent IHC was performed with the Tyramide Signal Amplification method using an Opal IHC kit (PerkinElmer, Waltham, MA) according to the instructions provided

by the manufacturer. Anti-human CD8 (clone C8/144b, DAKO), anti-human CD4 (clone 4B12, DAKO), anti-human CD3 (clone SP7, Abcam), anti-human FOXP3 (clone 236A/E7, Abcam) and anti-human PD-1 (clone EPR4877(2), Abcam) mAbs were used for primary staining. A horseradish peroxidase-labelled secondary detection system (EnVision plus, DAKO) was employed as a catalyst for fluorophore-conjugated tyramide. Multiplexed fluorescence-labelled images of randomly selected fields (669 x 500 μm each) were captured with an automated imaging system (Vectra ver. 3.0, PerkinElmer). Image analysis software (InForm, PerkinElmer) was used to segment cells and define specific phenotypes. Cells positive for CD8, CD4, FOXP3, and PD-1 were counted in three high-powered microscopic fields (400x; 0.0625 mm^2), and their averages were calculated. Two researchers (S. Kumagai and Y.O.) independently evaluated the stained slides.

Western blotting

Sub-confluent cells or tumors were washed with PBS and harvested with M-PER (Thermo Fisher Scientific). An 8-min Cytoplasmic & Nuclear Protein Extraction Kit (mammalian cells & tissues) (101 Bio, Mountain View, CA) was used for extraction of cytoplasmic and nuclear proteins from cultured lymphocytes. Cell lysates were separated by Sodium dodecyl sulfate-Polyacrylamide Gel Electrophoresis (SDS-PAGE) and blotted onto a polyvinylidene fluoride membrane. After blocking, the membrane was probed with the primary antibody. After rinsing twice with a tris-buffered saline (TBS) buffer, the membrane was incubated with a horseradish peroxidase-conjugated secondary antibody and washed, followed by visualization using an enhanced chemiluminescence (ECL) detection system and a LAS-4000 (GE Healthcare). The antibodies used for western blotting are summarized in key resources table. Each band intensity was given relative to the corresponding band intensity of β-actin or histone H3 and was quantified by ImageJ software (ver1.51) (Schneider et al., 2012).

Assay measuring LA concentration

To quantify LA concentration in culture, all cell lines were maintained in RPMI medium supplemented with 10% FBS. Blood plasma was subtracted from blood and interstitial fluids from tumors were collected by centrifugation as previously described (Wiig et al., 2003). The concentrations of LA were assessed with a Lactate Colorimetric/Fluorometric Assay Kit (BioVision, Milpitas, CA). Total LA content of clinical specimens was extracted and evaluated following the protocol which is offered by BioVision.

LC-MS assay for PEP

The cell suspension was transferred to a tube and centrifuged to spin-down the cells. The culture medium was aspirated from the tube, and the cells were washed with 10 mL of 5% mannitol solution. The cells were then treated with 800 μL of methanol and vortexed for 30 sec to suppress enzyme activity. Next, 550 μL of Milli-Q water containing internal standards (H3304-1002, Human Metabolome Technologies, Inc. (HMT), Tsuruoka, Yamagata, Japan) was added to the cell extract and vortexed for another 30 sec. The extract was then centrifuged at 2,300 ×g, 4°C for 5 min and 700 μL of the supernatant was centrifugally filtered through a Millipore 5-kDa cutoff filter (UltrafreeMC-PLHCC, HMT) at 9,100 ×g, 4°C for 120 min to remove macromolecules. Subsequently, the filtrate was evaporated to dryness under vacuum and reconstituted in 50 μL of Milli-Q water for metabolome analysis at HMT. Metabolome analysis was conducted according to HMT's ω Scan package, using capillary electrophoresis Fourier transform mass spectrometry (CE-FTMS) based on the methods described previously (Sasaki et al., 2019b). Briefly, CE-FTMS analysis was carried out using an Agilent 7100 CE capillary electrophoresis system equipped with a Q Exactive Plus (Thermo Fisher Scientific), an Agilent 1260 isocratic HPLC pump, an Agilent G1603A CE-MS adapter kit, and an Agilent G1607A CE-ESI-MS sprayer kit (Agilent Technologies). The systems were controlled by Agilent MassHunter workstation software LC/MS data acquisition for 6200 series TOF/6500 series Q-TOF version B.08.00 (Agilent Technologies) and Xcalibur (Thermo Fisher Scientific), and connected by a fused silica capillary (50 μm i.d. × 80 cm total length) with commercial electrophoresis buffer (H3301-1001 and I3302-1023 for cation and anion analyses, respectively, HMT) as the electrolyte. The spectrometer was scanned from m/z 50 to 1,000 in positive mode and from m/z 70 to 1,050 in negative mode, respectively (Sasaki et al., 2019b). Peaks were extracted using MasterHands automatic integration software (Keio University, Tsuruoka, Yamagata, Japan) to obtain peak information including m/z, peak area, and migration time (MT) (Sugimoto et al., 2010). Signal peaks corresponding to isotopomers, adduct ions, and other product ions of known metabolites were excluded, and the remaining peaks were annotated according to HMT's metabolite database based on their m/z values and MTs. Areas of the annotated peaks were then normalized to internal standards and sample volume to obtain relative levels of each metabolite. Hierarchical cluster analysis (HCA) and principal component analysis (PCA) (Yamamoto et al., 2014) were performed by HMT's proprietary MATLAB and R programs, respectively. Detected metabolites were plotted on metabolic pathway maps using VANTED software (Junker et al., 2006).

T cell culture with LA

CD45RA$^-$CD25^{high}CD4$^+$ T cells (eTreg cells) and CD8$^+$ T cells were sorted from PBMCs of healthy individuals using a FACSAria Fusion (BD Biosciences). A total of 1 × 10^4 each sorted T cells were stimulated with anti-CD3 mAb (clone: OKT3, Thermo Fisher Scientific) and anti-CD28 mAb (clone: CD28.2, Thermo Fisher Scientific) in the presence of 1 × 10^5 irradiated APCs and cultured in glucose-free RPMI medium (Thermo Fisher Scientific) supplemented with 10% dialyzed FBS, 10 IU/mL IL-2, 20 ng/mL IL-7, 1 mM glucose and the indicated concentration of LA (Sigma-Aldrich). In some wells, anti-PD-1 mAb (nivolumab) or control isotype-matched mAb was added. For murine experiments, CD8$^+$ T cells and Treg cells (CD25$^+$CD4$^+$ or Foxp3$^+$CD4$^+$ T cells) were purified from splenocytes of C57/BL6, *Slc16a1*$^{+/-}$, *Foxp3*^{Cre}, *Foxp3*^{Cre};*Slc16a1*$^{wt/fl}$ or *Foxp*^{Cre};*Slc16a1*$^{fl/fl}$ mice using autoMACS Pro Separator (Miltenyi

Biotec) or FACSAria Fusion (BD Biosciences). CD8$^+$ cells or Treg cells (1 × 10^4) were stimulated with anti-CD3 mAb and anti-CD28 mAb in the presence of 1 × 10^5 irradiated APCs and cultured in glucose-free RPMI medium (Thermo Fisher Scientific) supplemented with 10% dialyzed FBS, 10 IU/mL IL-2, 20 ng/mL IL-7, 1 mM glucose and the indicated concentration of LA (Sigma-Aldorich).

Suppression assay with murine T cells

CD8$^+$ T cells and Foxp3$^+$CD4$^+$ T cells (Treg cells) were prepared from splenocytes of *Foxp3*^{Cre} or *Foxp3*^{Cre};*Slc16a1*$^{fl/fl}$ mice using a FACSAria Fusion cell sorter. A total of 1 × 10^4 CFSE-labelled (1 μM) responder CD8$^+$ T cells (Tresp cells) from splenocytes were co-cultured with/without unlabelled Treg cells in the presence of 1 × 10^5 irradiated APCs (CD8$^-$CD4$^-$ cells) and 0.5 μg/mL anti-CD3 mAb under the indicated condition of culture medium. Proliferation was assessed 72h later by dilution of CFSE-labelled cells with FCM.

Suppression assay with human T cells

CD8$^+$ T cells and CD45RA$^-$CD25^{high}CD4$^+$ T cells (eTreg cells) were sorted from human healthy PBMCs using FACSAria Fusion. A total of 1 × 10^4 CFSE-labelled (1 μM) responder CD8$^+$ T cells (Tresp cells) from PBMCs were cocultured with/without unlabelled eTreg cells in the presence of 1 × 10^5 irradiated APCs (CD8$^-$CD4$^-$ cells) and 0.5 μg/mL anti-CD3 mAb under the indicated condition of culture medium. In some wells, anti-PD-1 mAb (nivolumab) or control isotype-matched mAb, and 100 nM of AR-C155858 or DMSO were added. Proliferation was assessed 72h later by dilution of CFSE-labelled cells with FCM.

QUANTIFICATION AND STATISTICAL ANALYSIS

GraphPad Prism7 (GraphPad Software, San Diego, California, USA), R version 4.1.0 and GSEA version 4.1.0 (Massachusetts Institute of Technology, Cambridge, MA) were used for statistical analyses. The relations between groups were compared using a t-test or a one-way ANOVA test. The relations between tumor volume curves were compared using a two-way ANOVA test. Survival was analyzed with the Kaplan-Meier method and was compared with the log-rank test. P values < 0.05 were considered statistically significant. For multiple testing, the Tukey's or Bonferroni's methods were employed.